Quantifying black carbon light absorption enhancement by a novel statistical approach

Cheng Wu[1,2], Dui Wu[1,2,3], Jian Zhen Yu[4,5,6]

[1]Institute of Mass Spectrometer and Atmospheric Environment, Jinan University, Guangzhou 510632, China

[2]Guangdong Provincial Engineering Research Center for on-line source apportionment system of air pollution, Guangzhou 510632, China

[3]Institute of Tropical and Marine Meteorology, China Meteorological Administration, Guangzhou 510080, China

[4]Division of Environment, Hong Kong University of Science and Technology, Clear Water Bay, Hong Kong, China

[5]Atmospheric Research Centre, Fok Ying Tung Graduate School, Hong Kong University of Science and Technology, Nansha, China

[6]Department of Chemistry, Hong Kong University of Science and Technology, Clear Water Bay, Hong Kong, China

Corresponding to: Cheng Wu (wucheng.vip@foxmail.com) and Jian Zhen Yu (jian.yu@ust.hk)

Abstract

Black carbon (BC) particles in the atmosphere can absorb more light when coated by non-absorbing or weakly absorbing materials during atmospheric aging, due to the lensing effect. In this study, the light absorption enhancement factor, E_{abs}, was quantified using one year's measurement of mass absorption efficiency (MAE) in the Pearl River Delta region (PRD). A new approach for calculating primary MAE (MAE_p), the key for E_{abs} estimation, is demonstrated using the Minimum R Squared (MRS) method, exploring the inherent source independency between BC and its coating materials. A unique feature of E_{abs} estimation by the MRS approach is its insensitivity to systematic biases in EC and σ_{abs} measurements. The annual average E_{abs550} is found to be 1.50±0.48 (±1 S.D.), exhibiting a clear seasonal pattern with higher values in summer and lower in the winter. Elevated E_{abs} in the rainy summer season is likely associated with aged air masses dominating from marine origin, along with long-range transport of biomass burning influenced air masses from Southeast Asia. E_{abs} induced by hygroscopic growth at elevated RH could be as high as 1.3. Core-shell Mie simulations along with measured E_{abs} and Angstrom absorption exponent (AAE) constraints suggest that in the PRD, the coating materials are unlikely to be dominated by brown carbon and the coating thickness is higher in the rainy season than the dry season. A negative correlation is found between $AAE_{470-660}$ and RH, suggesting a dominant particle size of D_{core} = 130 nm and D_{shell}/D_{core} range of 2 to 4.

1 Introduction

Originating from incomplete combustion, black carbon (BC) is a crucial constituent of atmospheric aerosols, and is an air pollutant itself, having an adverse health impacts on humans (Suglia et al., 2008). BC has also been recognized as the third most important climate forcer due to its broad light absorbing capability across the UV-Vis-IR spectrum (IPCC, 2013). BC can alter the climate in a variety of ways, including by direct forcing (Bond et al., 2011), affecting cloud cover (Koch and Del Genio, 2010) and precipitation (Tao et al., 2012), reducing the albedo of snow and ice (Hansen and Nazarenko, 2004) and causing surface dimming (Wild, 2011). The climate effects of BC can be global or regional (Ramanathan and Carmichael, 2008). A recent study found BC can modify planetary boundary layer meteorology, and thus enhance local pollution indirectly (Ding et al., 2016). However, due to its variable optical characteristics induced during atmospheric aging, large uncertainties still exist in estimating the radiative forcing from BC. Optical properties of BC can be predicted by knowing the mass concentration, mixing state and size distribution, which collectively serve as the cornerstone for modeling the climate effect of BC. In 3D modeling studies, to conserve computational resources, the mass absorption efficiency (MAE) or mass absorption cross-section (MAC) is widely used to convert black carbon mass concentration to light absorption coefficient (σ_{abs}). MAE is a quantity to describe the light absorption ability per unit EC mass:

$$\text{MAE } (m^2\ g^{-1}) = \frac{absorption\ coefficient\ \sigma_{abs}\ (Mm^{-1})}{EC\ mass\ concentration\ (\mu g\ m^{-3})} \tag{1}$$

As a fundamental input parameter, MAE has a critical impact on BC's radiative forcing estimation in climate modeling studies. Mixing state is one of the governing factors affecting MAE. Light absorption of soot particles is enhanced when coated with non-absorbing materials (Fuller et al., 1999) or weakly absorbing materials (Lack and Cappa, 2010) during atmospheric aging. The coating materials can focus more light onto the soot core through the lensing effect, resulting in elevated MAE (Wang et al., 2017). Strong correlations between MAE and the number/volume fraction of coated particles have been reported in urban areas like Tokyo (Naoe et al., 2009), Shenzhen (Lan et al., 2013) and Xi'an (Wang et al., 2014), implying that the elevated MAE observed at these locations was mainly due to the elevated fraction of coated of soot particles. Total absorption ($\sigma_{abs,t}$) of coated particles can

be separated into two parts: primary absorption ($\sigma_{abs,p}$) due to the uncoated soot core alone, and extra absorption ($\sigma_{abs,c}$) due to lensing effect of the coating (Bond et al., 2006; Jacobson, 2006; Liu et al., 2016a) and the presence of secondarily formed brown carbon (BrC) (Lack and Cappa, 2010; Liu et al., 2016b).

$$\sigma_{abs,t} = \sigma_{abs,p} + \sigma_{abs,c} \tag{2}$$

The absorption enhancement factor (E_{abs}) then can be defined as ratio of the total absorption and primary absorption coefficients or the corresponding MAE values:

$$E_{abs} = \frac{\sigma_{abs,t}}{\sigma_{abs,p}} = \frac{MAE_t}{MAE_p} \tag{3}$$

Where MAE_p represents the ratio of $\sigma_{abs,p}/EC$ for uncoated soot particles, similar to the concept of the primary OC/EC ratio in the EC tracer method:

$$MAE_p = \frac{\sigma_{abs,p}}{EC} \tag{4}$$

And the MAE of coated BC can be defined as:

$$MAE_t = \frac{\sigma_{abs,t}}{EC} \tag{5}$$

Thus, elevated MAE induced by coating during atmospheric aging results in an E_{abs} larger than 1.

Previous model studies suggest that absorption by aged soot particles can be 1.5 times greater than fresh soot (Fuller et al., 1999; Bond et al., 2006). Laboratory studies have demonstrated that soot particles coated with SOA (Saathoff et al., 2003; Schnaiter et al., 2005) and sulfuric acid (Zhang et al., 2008; Khalizov et al., 2009) can increase E_{abs}. An artificial coating experiment by Shiraiwa et al. (2010) found an E_{abs} of 2 for graphite particles growing in diameter from 185 to 370 nm. A laboratory study by McMeeking et al. (2014) found that in the presence of BrC, light absorption enhancement is more pronounced at the shorter wavelength. A recent chamber study coupling actual ambient air with seed BC particles implies that the timescale for E_{abs} reaching 2.4 is only 5 hours in Beijing but 18 hours in Houston (Peng et al., 2016). Field studies conducted in recent years have also substantiated enhanced light absorption in Canada (Knox et al., 2009; Chan et al., 2011), US (Lack et al., 2012b), UK (Liu et al., 2015) and Japan (Nakayama et al., 2014; Ueda et al., 2016). In contrast, field studies in California,

87   US (Cappa et al., 2012) found a weaker light absorption enhancement (6% on average). A recent study

88   suggests the mass ratio of non-BC content to BC particles determines the occurrence of the absorption

89   enhancement of black-carbon particles (Liu et al., 2017).

90   Two approaches are widely used to determine E_{abs} from ambient measurements. The first approach

91   removes the coating materials on particles physically using a thermal denuder (TD) (Lack et al., 2012a)

92   or by aerosol filter filtration-dissolution (AFD) (Cui et al., 2016b). The TD approach is briefly

93   discussed here. Coating materials can be removed by TD at a working temperature around 200 to

94   300 °C (depending on the charring characteristics of aerosols at the sampling site) to measure $\sigma_{abs,p}$,

95   which are cycled with measurements of $\sigma_{abs,t}$ (without passing through TD), allowing E_{abs} to be

96   obtained from the ratio of $\sigma_{abs,t}/\sigma_{abs,p}$ following Eq.3. The major advantage of the TD approach is

97   its ability to provide highly time resolved measurements (minutes). A photo-acoustic spectrometer

98   (PAS) is commonly used with TD for detection to satisfy its high time resolution demands. As an in-

99   situ technique, PAS eliminates the artifacts associated with filter-based methods (Weingartner et al.,

100   2003; Coen et al., 2010) and is often considered as the reference instrument for light absorption

101   coefficient determination (Arnott et al., 2003; Arnott et al., 2005). One limitation of the TD approach is

102   that a universal optimal operation temperature does not exist. If the temperature is too low, the coating

103   cannot be fully removed, and charring can occur if the TD temperature is too high, leading to biased

104   results. Another issue is particle loss due to TD, which can be ~ 20% and needs to be taken into account

105   (Ueda et al., 2016). It's also worth noting that MAE_p by the TD approach is different from the MAE_p

106   at the emission source. First, the morphology of thermally denuded BC particles (compact aggregates)

107   is different from that of freshly emitted BC particles (chain-like aggregates). Second, most of the

108   coatings is removed with the TD denuded soot particles, but freshly emitted soot particles usually

109   come with a thin coating of OC formed from condensation of OC vapors as the temperature drops

110   from engine to the ambient air. As a result, the MAE_p by TD approach is expected to be lower than

111   the MAE_p of emission source. In this sense, the TD approach may not be a prefect "time machine" to

112   reverse the aging process for E_{abs} determination.

113   The second approach is the MAE ratio method, which is also stated in Eq. 3. The key to this method

114   is determining an appropriate MAE_p that can represent the MAE from primary emissions. One

approach is to adopt the reference MAE_p from the literature but it may fail to represent the actual MAE_p at a specific sampling site, since MAE_p varies temporally and spatially. For example, MAE_p of diesel soot was found to be 7.1 m^2g^{-1} at 532 nm (Adler et al., 2010). A much higher MAE_p (16 m^2g^{-1} at 530 nm) was observed from natural gas flaring (Weyant et al., 2016). MAE_p of biomass burning (BB) samples is highly varied due to a wide range of fuel types and combustion conditions (Reid et al., 2005; Roden et al., 2006). A range from 6.1 to 80.8 m^2g^{-1} was reported for BB MAE_p at 550 nm (Pandey et al., 2016). Without the knowledge of source contributions, it is not feasible to derive a representative MAE_p for E_{abs} estimation. The other commonly used approach is to determine MAE_p from the dependency of MAE on the number fraction of coated soot particles measured by SP2 (Lan et al., 2013). Since MAE (y axis) is positively correlated with the number fraction of coated soot particles (x axis), MAE_p can be determined by extending the regression line to x=0. It is worth noting that this approach provides only a rough approximation of E_{abs} since the parameter used here (coated soot particles number fraction) ignores other main drivers of light absorption enhancement (e.g. coating thickness). As a result, this approach is only valid for a period of measurements, for which coating thickness is relatively constant and the MAE variations are dominated by coated soot particles number fraction.

However, the high cost of the TD-PAS system and SP2 limit the field measurement of E_{abs} around the world. In addition, long-term E_{abs} measurements by a TD-PAS system and SP2 are not easily achieved and rarely reported. On the other hand, an Aethalometer and RT-ECOC analyzer can be effectively deployed for long term measurements and E_{abs} estimation, at a relatively lower cost. In this study, based on one year of hourly MAE measurements (with the field carbon analyzer and Aethalometer) at a suburban site in the Pearl River Delta (PRD) region of China, quantification of MAE_p is demonstrated by a novel statistical approach, the Minimum R squared method (MRS) (Wu and Yu, 2016). The aim of this study is to demonstrate the capability of E_{abs} estimation using a year-long dataset from cost-effective instrumentation. The seasonal variability of MAE, AAE and E_{abs} in the PRD region are characterized and their dependency on air mass origin, biomass burning and RH are discussed. Abbreviations used in this study are summarized in Table 1 for a quick lookup.

2 Ambient measurements

Sampling was conducted from Feb 2012 to Jan 2013 at the suburban Nancun (NC) site (23° 0'11.82"N, 113°21'18.04"E). NC, situated on the top of the highest peak (141 m ASL) in Guangzhou's Panyu district, is located at the geographic center of the PRD region, making it a representative location for average atmospheric mixing characteristics of city clusters in the PRD region. Light absorption measurements were performed by a 7-λ Aethalometer (AE-31, Magee Scientific Company, Berkeley, CA, USA). The Aethalometer was equipped with a 2.5 μm cyclone with a sampling flow rate of 4 L min^{-1}. Weingartner's algorithm (Weingartner et al., 2003) was adopted to correct the sampling artifacts (aerosol loading, filter matrix and scattering effect) rooted in filter based method. A customized Aethalometer data processing program (Wu, 2017a) with graphical user interface was developed to perform data correction and detailed descriptions can be found in the SI (The program is available from https://sites.google.com/site/wuchengust). Details of the Aethalometer setup and data correction can be found in our previous paper (Wu et al., 2013).

EC mass concentrations were determined by a real time ECOC analyzer (Model RT-4, Sunset Laboratory Inc., Tigard, Oregon, USA). The sunset carbon analyzer was sampling on hourly cycles at a flow rate of 8 Lmin^{-1} with a PM$_{2.5}$ sharp-cut cyclone inlet. For each measurement hour, the first 45min were for sample collection and the remaining 15 min for thermal-optical analysis. OC is volatized first by step-wise temperature ramping in an oxygen-free atmosphere while in the second stage EC is combusted in the presence of oxygen. Laser transmittance is applied to correct the charring artifact during the OC stage.

Considering a measurement precision of 5% for the Aethalometer (Hansen, 2005) and 24% for the RT-ECOC analyzer (Bauer et al., 2009), the propagated relative precision of E$_{abs}$ ($E_{abs,Unc}$) is 35% following Eq. S1&S2 in the SI. It should be noted that $E_{abs,Unc}$ is mainly attributed to the measurement precision of EC by the RT-ECOC analyzer. Since the measurement precision of the RT-ECOC analyzer estimated by Bauer et al. (2009) is obtained from field measurement at an environment (EC below 1 μg m^{-3}) where EC is much lower than the present study (annual average EC 2.66±2.27 μg m^{-3}), the $E_{abs,Unc}$ of 35% should be considered as an upper limit for the present study.

169   Light scattering was measured by an integrating nephlometer (Aurora-1000, Ecotech, Melbourne,

170   Australia). Water soluble ions were measured by MARGA (The instrument for Measuring AeRosols

171   and GAses)(ten Brink et al., 2007). Both instruments are equipped with a PM$_{2.5}$ inlet to remove the

172   coarse particles.

173   2.1 Uncertainties of MAE determination

174   Two major uncertainties associated with the σ_{abs} and EC determination techniques should be taken

175   into account when comparing MAE across different studies. For the σ_{abs} determination technique,

176   photo-acoustic spectroscopy (PAS) is an in-situ technique free from filter based artifacts, but its

177   application is limited by its high cost. The filter based optical transmittance method (e.g., Aethalometer

178   and Multi Angle Absorption Photometer, MAAP) is the most widely used technique around the world,

179   but data correction is needed to minimize the bias from artifacts due to the loading effect, matrix effect

180   and scattering effect (Weingartner et al., 2003; Arnott et al., 2005; Schmid et al., 2006; Virkkula et al.,

181   2007; Coen et al., 2010; Drinovec et al., 2017; Saturno et al., 2017). Besides these artifacts, RH is also

182   a source of σ_{abs} measurement uncertainty. Elevated RH is not only a driving force of increased σ_{abs}

183   due to the hygroscopic growth of particles, but also a factor affecting ambient σ_{abs} measurements.

184   Previous studies found σ_{abs} by PAS exhibit a systematic decrease when RH>70% (Arnott et al., 2003;

185   Kozlov et al., 2011). Water evaporation was found as the major cause for the biased PAS σ_{abs}

186   measurements under high RH (Raspet et al., 2003; Lewis et al., 2009b; Langridge et al., 2013). Filter-

187   based measurements are also affected under high RH conditions. For example, Arnott et al. (2003)

188   observed erratic responses by particle soot absorption photometer (PSAP) as RH changed. The main

189   reason is traced to the hydrophilic cellulose membrane, which serves to reinforce the quartz filter used

190   in PSAP. The fibers can swell and shrink as RH changes, causing unwanted light attenuation signal.

191   The PTFE-coated glass-fiber tape has become available since 2012 for the recent model of

192   Aethalometer to minimize the RH interference (Magee-Scientific, 2017). A study by Schmid et al.

193   (2006) reported dependency of PSAP σ_{abs} on RH, but found negligible effect of RH on Aethalometer

194   performance. It is also worth noting that RH in the Aethalometer optical chamber may be lower than

195   the ambient RH due to the slightly elevated temperature inside the instrument. The magnitude of RH

196   difference was found similar between different instruments: 20% for the Aethalometer (Schmid et al.,

197   2006) and 15% for the nephelometer (Guyon et al., 2004). The RH in the Aethalometer optical chamber

198   was not measured in this study. We expected its level to be slightly lower than the ambient RH. Cappa

199   et al. (2008) found σ_{abs} measurements by PSAP and PAS maintained a high linearity even under high

200 RH conditions (65-91%). Inter-comparison studies demonstrated that with proper corrections,

201 Aethalometer σ_{abs} measurements agree well with those by PAS (Ajtai et al., 2011). During the inter-

202 comparison study of an Aethalometer (AE-16) and a PAS in Guangzhou (Wu et al., 2009), good

203 correlation was found (R^2=0.96) as shown in Figure S1. These comparison results imply that the

204 Aethalometer results are linearly correlated with PAS measurements and RH has a limited interference

205 on Aethalometer measurements. In our study, careful corrective measures (Wu et al., 2013) are

206 conducted for the Aethalometer σ_{abs} data treatment to minimize these artifacts. But such artifacts

207 still cannot be fully eliminated.

208 For the EC determination, different thermal optical analysis (TOA) protocols can impact the

209 measurement variability and thus MAE. As shown in Table S1, MAE for the same samples at Fresno

210 varied from 6.1 to 9.3 $m^2\,g^{-1}$, depending on which EC analysis protocol was applied (Chow et al.,

211 2009). Studies in the PRD found that discrepancies in measured EC by different analysis protocols

212 could be as large as a factor of 5 (Wu et al., 2012; Wu et al., 2016a), which adds to the uncertainty for

213 the MAE estimation. In addition, EC by TOA is also different from refractory BC (rBC) reported by

214 the laser induced incandescence (LII) technique (e.g. single particle soot photometer, SP2). For

215 example, two studies in Toronto (Knox et al., 2009; Chan et al., 2011) both used the PAS for σ_{abs}

216 measurement but different techniques for EC mass determination, resulting in very different MAE

217 results. LII instruments are usually calibrated with a commercially available surrogate (e.g. fullerene)

218 since direct calibration with ambient soot is not easy to achieve. Laborde et al. (2012) indicates that

219 the incandescence response of SP2 exhibits a dependency on soot type (15% between fullerene and

220 denuded diesel soot particles; 14% between biomass burning and denuded diesel soot particles). Due

221 to the absence of widely accepted reference materials for EC, the uncertainties in EC determination

222 will exist in the foreseeable future. All these uncertainties, including the uncertainty of rBC mass

223 determination by SP2, uncertainty of EC in TOA, the discrepancy between SP2 rBC and TOA EC and

224 the discrepancy of σ_{abs} between filter transmission and photo-acoustic methods, can contribute to the

225 differences in MAE listed in Table S1.

226 Systematic bias in MAE (e.g. overestimation of σ_{abs} and variability of EC mass by different

227 TOA protocols) discussed above have little effect on E_{abs} estimation by MRS. As shown in Eq. 3, E_{abs}

228   is the ratio of MAE_t to MAE_p or $\sigma_{abs,t}$ to $\sigma_{abs,p}$, thus most of the bias in EC mass or σ_{abs} is

229   cancelled out during the E_{abs} calculation. More details are discussed in section 4.1.

230   **3 Methodology**

231   **3.1 MAE_p estimation by MRS from the ambient data**

232   In this section, a new approach for MAE_p estimation is introduced for E_{abs} determination, which

233   requires the knowledge of differentiating $\sigma_{abs,p}$ and $\sigma_{abs,c}$ portions in $\sigma_{abs,t}$. The idea of

234   decoupling $\sigma_{abs,t}$ into $\sigma_{abs,p}$ and $\sigma_{abs,c}$ is conceptually similar to decoupling OC into primary OC

235   (POC) and secondary OC (SOC) in the EC tracer method as shown in Table 2. In the EC tracer method,

236   if $(OC/EC)_p$ is known, POC can be determined from OC (Turpin and Huntzicker, 1991). The role of

237   MAE_p here is similar to the role of $(OC/EC)_p$, the primary OC/EC ratio in the EC tracer method (a

238   comparison is given in Table 2). If MAE_p (average MAE from primary emission sources) is known,

239   E_{abs} can be obtained from the ratio of MAE_t/MAE_p (Eq. 3). Therefore, the key for E_{abs} estimation is to

240   derive an appropriate MAE_p. It is worth noting that MAE_p here does not represent MAE from a single

241   or specific primary emission source, instead it reflects an average and effective MAE that has taken

242   consideration of various primary emission sources. Thus, the MAE_p is conceptually analogous to

243     $(OC/EC)_p$ in the EC tracer method, in which the primary ratio reflects an overall ratio from primary

244   emission sources rather than from a single primary source.

245   The Minimum R squared method (MRS) explores the inherent independency between

246   pollutants from primary emissions (e.g., EC) and products associated with secondary formation

247   processes (e.g., SOC, $\sigma_{abs,c}$) to derive the primary ratios (e.g., $(OC/EC)_p$, MAE_p) in the EC tracer

248   method (Wu and Yu, 2016). When applying MRS for light absorption enhancement estimation, MRS

249   is used to explore the inherent independency between EC and $\sigma_{abs,c}$, which is gained during

250   atmospheric aging after emission. An example of MAE_p estimation by MRS is shown in Figure 1.

251   Firstly, the assumed MAE_p value is varied continuously in a reasonable range (0.01 to 50 $m^2\ g^{-1}$ as

252   shown in Figure 1). Then at each hypothetical MAE_p, $\sigma_{abs,c}$ can be calculated by Eq. 6 (a combination

253   of Eq. 2&4) using EC and $\sigma_{abs,t}$ from ambient measurements.

$$\sigma_{abs,c} = \sigma_{abs,t} - MAE_p \times EC \qquad (6)$$

Accordingly, for each hypothetical MAE_p, a correlation coefficient value (R^2) of $\sigma_{abs,c}$ vs. EC (i.e., $R^2(\sigma_{abs,c}, EC)$) can be obtained. The series of $R^2(\sigma_{abs,c}, EC)$ values (y axis) are then plotted against the assumed MAE_p values (x axis) as shown by the red curve in Figure 1. The physical meaning of this plot can be interpreted as follows. The $\sigma_{abs,p}$ is the fraction of light absorption owing to primary emitted soot particles. As a result, $\sigma_{abs,p}$ is well correlated with EC mass. In contrast, the $\sigma_{abs,c}$ is the fraction of light absorption gained by the lensing effect of the coating on particles after emission. The variability of $\sigma_{abs,c}$ mainly depends on the coating thickness of the soot particles. Consequently, $\sigma_{abs,c}$ is independent of EC mass. Since variations of EC and $\sigma_{abs,c}$ are independent, the assumed MAE_p corresponding to the minimum $R^2(EC, \sigma_{abs,c})$ would then represent the most statistically probable MAE_p of the tested dataset.

A computer program (Wu, 2017b) in Igor Pro (WaveMetrics, Inc. Lake Oswego, OR, USA) was developed to facilitate MRS calculation with a user friendly graphical user interface. Another two Igor Pro based computer programs Histbox (Wu, 2017c) and Scatter Plot (Wu, 2017d) are used for generating histograms, box plots and scatter plots (with Deming regressions) presented in this study. Detailed descriptions of these computer programs can be found in the SI and the computer programs are available from https://sites.google.com/site/wuchengust.

3.2 Mie simulation

It can be informative to model a single soot particle using Mie theory (Bohren and Huffman, 1983) and understand the theoretical range and variability of the soot particle's optical properties. Three types of mixing state are widely employed for parameterization: internal mixing, external mixing and core-shell. To better represent the real situation (coating due to the aging process), a core-shell model is considered in the Mie calculation (Figure S2), which is more realistic than a volume mixture model (Bond et al., 2006). An aerosol optical closure study in the North China Plain (NCP) found that the core-shell model can provide better performance than assuming purely internal mixing and external mixing (Ma et al., 2012). A morphology study using Scanning Transmission X-ray Microscopy found that core-shell is the dominating mixing state in ambient samples (Moffet et al.,

281   2016). It should be noted that the core-shell model assumption still has its own limitations. A single

282   particle soot photometer (SP2) study by Sedlacek et al. (2012) reported a negative lag time between

283   the scattering and incandescence signals in samples influenced by biomass burning, implying   a near

284   surface location of soot relative to non-absorbing materials. Near surface type mixing of soot has also

285   been observed in Tokyo, but accounted for only 10% of total mixed soot containing particles (Moteki

286   et al., 2014). Considering the domination of core-shell type particles in the ambient environment, the

287   core-shell assumption in our optical model is sufficient to approximate the real situation.

288   As shown in Figure S2, fresh emitted soot particles are chain-like aggregates of small spheres

289   (30~50 nm). After the aging process, soot particles are coated with organic and inorganic materials.

290   Sufficient evidence has shown that the coating not only results in particle size growth, but also makes

291   the soot core become more compact due to its collapse (Alexander et al., 2008; Zhang et al., 2008;

292   Lewis et al., 2009a), especially under high RH conditions (Leung et al., 2017). Since the spherical like

293   core and shell favor Mie simulation, both core and shell are considered as spheres in the Mie

294   calculation.

295   To investigate the spectrum properties of soot particles, 11 wavelengths (370, 405, 470, 520,

296   532, 550, 590, 660, 781, 880 and 950 nm) are considered in calculations to cover wavelengths in the

297   most frequently used absorption measurement instruments. A refractive index (RI) of $1.85 - 0.71i$ is

298   adopted for soot core (Bond and Bergstrom, 2006) and 1.55 for non-absorbing coating (clear shell) in

299   the Mie calculation for all wavelengths. Studies suggest a group of organic matter (OM), known as

300   Brown Carbon (BrC), can absorb solar radiation at UV wavelengths (Kirchstetter et al., 2004). Thus,

301   a BrC coating (brown shell) scenario is also considered in Mie simulation following the wavelength-

302   dependent RI suggested by Lack and Cappa (2010), which ranges from 1.55-0.059i (370 nm) to 1.55-

303   0.0005i (950 nm). A modeling study by Bond et al. (2006) indicates that absorption amplification is

304   not sensitive to the RI, thus the result below is not expected to be sensitive to the RI variability. Due

305   to the spherical assumption of the BC core, a constant particle density is adopted for simplicity instead

306   of size dependent particle density. But it is worth noting that in reality, the effective density of soot

307   varies with particle size due to the morphology change during particle aging (Tavakoli and Olfert,

308   2014; Dastanpour et al., 2017). Both core diameters (D_{core}) and shell diameters (D_{shell}) are constrained

309 in the range of 10 ~ 3000 nm in the model simulations. The Mie calculations are implemented with a

310 customized program (Wu, 2017e) written in Igro Pro (WaveMetrics, Inc. Lake Oswego, OR, USA)

311 and it is available from https://sites.google.com/site/wuchengust. It should be noted that the core-shell

312 type mixing state of particles is still rare in 3D atmospheric models like WRF-Chem (Matsui et al.,

313 2013; Nordmann et al., 2014) due to computational cost limitation.

3.2.1 Mie modeled absorption angstrom exponent (AAE)

315 Absorption Angstrom Exponent (AAE) is a widely used parameter that describes the

316 wavelength dependence of aerosol light absorption (Moosmuller et al., 2011), which can be written

317 explicitly as

$$AAE(\lambda_1, \lambda_2) = -\frac{\ln(\sigma_{abs,\lambda1}) - \ln(\sigma_{abs,\lambda2})}{\ln(\lambda_1) - \ln(\lambda_2)} \qquad (7)$$

319 It is well known that ambient soot particles exhibit an AAE close to unity (Bond, 2001).

320 Modeled variability in $AAE_{470-660}$ of bare soot particles is shown in Figure S3. For soot particles with

321 D_{core} <200 nm, $AAE_{470-660}$ is very close to 1 and decreases significantly for particles with D_{core} >200

322 nm. Considering a typical D_{core} of fresh emitted soot particles smaller than 200 nm (Rose et al., 2006;

323 China et al., 2013), the model results confirm the frequently observed AAE close to 1 from ambient

324 measurements (Kirchstetter et al., 2004). Modeled variability in $AAE_{470-660}$ of soot particles coated by

325 non-absorbing substances (clear shell) and weakly absorbing materials (brown shell) is shown in

326 Figure 2. Elevated AAE to ~2 is observed in the clear shell scenario (Figure 2a and 3b) for the most

327 probable soot core particle sizes (<200 nm), which agrees well with a previous model study (Lack and

328 Cappa, 2010), implying that elevated AAE cannot be exclusively attributed to mixing with BrC. AAE

329 elevation is more pronounced in the brown shell scenario. For soot particles with D_{core} <200 nm, brown

330 shell $AAE_{470-660}$ can easily reach 3 for a coating of D_{shell}/D_{core}=3 (Figure 2c and 2d). These high AAE

331 results are consistent with the previous model study (Lack and Cappa, 2010) and could partially

332 explain the high AAE observed in measurement studies (Kirchstetter et al., 2004; Hoffer et al., 2006),

333 since the presence of externally mixed BrC particles also contribute to the wavelength dependent light

334 absorption.

3.2.2 Mie modeled single scattering albedo (SSA)

Variability in modeled SSA of soot particles coated by non-absorbing substances and weakly absorbing materials (e.g. BrC) is shown in Figure S4. For particles with D_{core}<200 nm and D_{shell}/D_{core} <3, the SSA increases gradually (up to ~0.9) with a thicker coating and behaves similarly between clear shell and brown shell scenarios.

3.2.3 Mie modeled mass absorption efficiency (MAE)

MAE is a useful indicator for soot mixing state. Variability in MAE of bare soot particles as a function of particle size at a wavelength of 550 nm is illustrated in Figure S5. The magnitude of MAE is sensitive to the soot density assumption, especially for particles <200 nm (Figure S5), but the overall trend of particle size dependency is similar between different density scenarios. MAE peaks at a particle size of 200 nm and decreases dramatically for larger particles. In our MAE calculation, a soot density of 1.9 g cm^{-3} is adopted, as suggested by Bond and Bergstrom (2006). The purpose of adopting constant density is to simplify the MAE calculation. It should be noted that the effective density of soot core is highly variable in ambient environments. For example, a study in Beijing (Zhang et al., 2016b) found a value of 1.2 g cm^{-3}. A recent chamber study found the effective density of soot can evolve from 0.43 to 1.45 g cm^{-3} during aging as coated by m-Xylene oxidation products (Guo et al., 2016). A study by a single-particle aerosol mass spectrometer in Guangzhou found the effective density of soot increased with particle size in the range of 400 to 1600 nm (Zhang et al., 2016a). The MAE of coated particles from different core/shell diameter combinations are shown in Figure S6. For thickly coated particles, the MAE in the clear shell scenario varied as D_{shell}/D_{core} increased, but the MAE of brown shell scenario increased quasi-monotonously with D_{shell}/D_{core}.

3.2.4 Mie modeled light absorption enhancement factor (E_{abs})

E_{abs} is a better indicator for soot mixing state than MAE since it does not rely on the soot density assumption and is more suitable for comparing Mie simulations with ambient measurements. Modeled variability in E_{abs} of soot particles coated by non-absorbing substances and weakly absorbing materials

360   (e.g. BrC) is shown in Figure 3a and 3c respectively. E_{abs} is not only sensitive to the core/shell diameter

361   combination, but also behaves very differently on the clear and brown shell assumptions. For the clear

362   shell scenario, when D_{coat}/D_{core} <2, E_{abs} does not exceed 2 for particles with different soot core sizes,

363   but for the same D_{coat}/D_{core}, a larger soot core size yields a higher E_{abs} (Figure 3b, cross-sections of

364   Figure 3a). If D_{coat}/D_{core} >2, E_{abs} could be 3 to 5 for particles with a soot core smaller than 200 nm, but

365   for particles with a soot core larger than 200 nm, the E_{abs} is limited to ~2 as shown in Figure 3b. For

366   the brown shell scenario, E_{abs} increased quasi-monotonically with D_{coat}/D_{core}, and this trend is similar

367   for different soot core sizes (Figure 3d). The main reason behind is that in the brown shell scenario,

368   both lensing effect and BrC absorption contribute to E_{abs}. As shown in Figure S7, the BrC absorption

369   contribution to total E_{abs} strongly depends on coating thickness and is insensitive to soot core diameters.

370   When the coating is relatively thin (<5 nm for λ@370 nm, <15 nm for λ@550 nm and <40 nm for

371   λ@880 nm), BrC absorption contribution to the total E_{abs} is less than 20%. As the coating increases to

372   a certain level (~15 nm for λ@370 nm, ~35 nm for λ@550 nm and ~90 nm for λ@880 nm), BrC

373   absorption contribution is comparable to the lensing effect contribution, each contributing ~50% to

374   the total E_{abs}. When the BrC coating is sufficiently thick (>30 nm for λ@370 nm, >90 nm for λ@550

375   nm and >110 nm for λ@880 nm), BrC absorption dominates the E_{abs} contribution. As a result, if BrC

376   coating is indeed present in ambient samples, a strong wavelength dependent E_{abs} could be observed,

377   since a BrC coating of 30 nm would be enough to induce a large amount of detectable E_{abs} in the UV

378   range. Another major difference between the clear and brown shell scenarios is that, for thickly coated

379   particles (e.g. D_{coat}/D_{core} >2), the brown shell can yield a much higher E_{abs} than the clear shell.

380   Both primary soot size distribution and coating thickness can affect the absorption

381   enhancement of ambient BC particles. Ambient measurements by LII found soot particle number and

382   mass modes peaking at 110 nm and 220 nm, respectively, in the PRD (Huang et al., 2011b). A study

383   in Shanghai found similar results (70 nm for number concentrations and 200 nm for mass

384   concentrations)(Gong et al., 2016). Considering that the LII technique is specific for BC mass

385   determination which is independent of BC mixing state, the size distribution reported by LII can

386   represent the size distribution of the BC core. A study using a Micro Orifice Uniform Deposit Impactor

387   (MOUDI) found a EC mass size distribution in the PRD exhibiting three modes peaking at ~300, ~900

388 and ~5000 nm (Yu et al., 2010), implying a substantial coating of BC particles, and a diameter

389 amplification of 3. BC sizing by LII is based on volume equivalent diameter (VED), while MOUDI is

390 based on aerodynamic diameter. As a result, these two techniques do not necessarily yield similar sizes,

391 even for the bare soot particles. The conversion between these two types of diameters involves the

392 knowledge of particle density and morphology (drag force). A recent closure study on BC mixing state

393 in the PRD region suggests σ_{abs} is dominated by coated soot particles in the range of 300~400 nm

394 (Tan et al., 2016). Considering the dominant BC core distribution measured by SP2 (110 nm), the

395 upper limit of E$_{abs}$ in the PRD is roughly estimated as ~2 for the clear shell scenario (Figure 3b).

4 Results and discussions

4.1 Annual measurement statistics

398 The frequency distribution (log-normal) of σ_{abs550} is shown in Figure 4a, with an annual average (±1

399 S.D.) of 42.65±30.78 Mm^{-1}. A log-normal distribution is also found in the EC mass concentration

400 (Figure 4b), with an annual average of 2.66±2.27 µg m^{-3}. Figure 4c demonstrates the yearlong

401 frequency distribution of MAE$_{550}$ at the NC site. The annual average MAE$_{550}$ is 18.75±6.16 m^2 g^{-1} and

402 the peak (±1 S.D.) of the lognormal fit is 15.70±0.22 m^2 g^{-1}. A good correlation is observed between

403 σ_{abs} and EC mass (R^2=0.92) as shown in Figure 4d, and the color coding indicates a MAE dependency

404 on RH (the RH effect will be discussed in section 4.5). Annual average AAE$_{470-660}$ is 1.09±0.13 (Figure

405 S8a), indicating that soot is the dominant absorbing substance in the PRD and the brown shell scenario

406 shown in the Mie simulation is unlikely to be important. Annual mean SSA$_{525}$ is 0.86±0.05 (Figure

407 S8c), similar to previous studies in the PRD (Jung et al., 2009; Wu et al., 2009). For comparison

408 purpose, MAE measured at original wavelength and MAE scaled to 550 nm following the λ^{-1}

409 assumption are both shown in Table S1. The MAE comparisons discussed below are MAE at 550 nm.

410 MAE$_{550}$ by previous studies at various locations was found to cover a wide range, from 5.9 to 61.6 m^2

411 g^{-1}. Annual average observed MAE$_{550}$ at NC (18.75 m^2 g^{-1}) is higher than many studies shown in Figure

412 5, e.g., Shenzhen (Lan et al., 2013), Beijing (Yang et al., 2009), Mexico city (Doran et al., 2007) and

413 Fresno (Chow et al., 2009).

As shown in Figure 1, the annual average $MAE_{p,550}$ estimated by MRS is 13 $m^2 g^{-1}$. MAE_p by MRS represents the MAE_p at the emission source, which is different from the MAE_p by the TD approach for two reasons. First, the morphology of thermally denuded BC particles (compact aggregates) is different from that of freshly emitted BC particles (chain-like aggregates). Second, most of the coatings are removed for TD denuded soot particles, but freshly emitted soot particles usually come with a thin coating of OC formed from condensation of OC vapors as the temperature drops from the flame to the ambient air. As a result, the MRS-derived MAE_p is expected to be higher than the MAE_p by the TD approach. The estimated $MAE_{p,550}$ is higher than a previous study in Guangzhou (7.44 $m^2 g^{-1}$) (Andreae et al., 2008), but comparable to Xi'an (11.34 $m^2 g^{-1}$) (Wang et al., 2014) and Toronto (9.53~12.57 $m^2 g^{-1}$) (Knox et al., 2009). The annual average E_{abs550} by MRS following Eq. 3 is estimated to be 1.50±0.48 (mean ± 1 S.D.).

It should be noted that the E_{abs} estimation approach demonstrated here is insensitive to the MAE bias (e.g. overestimation of σ_{abs} and variability of EC mass by different TOA protocols) discussed in section 2.1, because bias in EC mass or σ_{abs} is cancelled out in the E_{abs} calculation (Eq. 3), since E_{abs} is the ratio of $\sigma_{abs,t}$ to $\sigma_{abs,p}$. To investigate the performance of the MRS approach in response to systematic bias in EC and σ_{abs}, two simple tests are conducted as shown in Figures S9 and S10 by adding systematic biases to σ_{abs550} and EC. Test A represents a situation when σ_{abs} is overestimated and EC is underestimated. The biased data are marked as σ'_{abs550} and EC' respectively, as shown below:

$$\sigma'_{abs550} = \sigma_{abs550} \times 2 \tag{8}$$

$$EC' = EC \times 0.7 \tag{9}$$

As a result, the average MAE_{550} changed from 18.75 to 53.58 $m^2 g^{-1}$ and MAE_p changed from 13 to 37 $m^2 g^{-1}$ (Figure S9). However, E_{abs} by ratio of averages remain the same (1.44).

In Test B, EC by different TOA protocols are compared to investigate the effect of different EC determination approaches while σ_{abs550} remains unchanged. EC by IMPROVE TOR protocol is calculated from NIOSH TOT EC following an empirical formula for suburban sites derived from a 3-year OCEC dataset in PRD (Wu et al., 2016a):

$$EC_{IMP\_TOR} = 2.63 \times EC_{NSH\_TOT} + 0.05 \tag{10}$$

442 As shown in Figure S10, MAE_{550} changed from 18.75 to 7.02 $m^2\,g^{-1}$ and MAE_p changed from 13 to 5

443 $m^2\,g^{-1}$, but E_{abs} remain almost the same (1.40). Result of Test B implies that although EC is

444 operationally defined, the discrepancy of EC between TOA protocols did not weaken the role of EC

445 serving as a tracer for primary emissions in MRS application. These examples demonstrate that

446 systematic biases in σ_{abs550} and EC have no effects on E_{abs} estimation by the MRS approach.

447 As mentioned in section 1, the definition of MAE_p by the TD approach is different from the

448 MAE_p of emission source. The TD MAE_p is expected to be slightly lower than the MAE_p of emission

449 source. Therefore, the corresponding E_{abs} are slightly different and it should be cautioned when

450 comparing MRS-derived E_{abs} with E_{abs} by the TD approach and Mie simulations. The E_{abs} could vary

451 by location, depending on the coating thickness and size distribution of the primary aerosols. After

452 undergoing atmospheric aging, the E_{abs} can be increased during transport from emission source to rural

453 areas. The magnitude of the E_{abs} found at the NC site is comparable to other locations such as Boulder

454 (Lack et al., 2012a) (1.38), London (Liu et al., 2015) (1.4), Shenzhen (Lan et al., 2013) (1.3), Yuncheng

455 (Cui et al., 2016b) (2.25), Jinan (Chen et al., 2017) (2.07) and Nanjing (Cui et al., 2016a) (1.6) and is

456 higher than studies in California (Cappa et al., 2012) (1.06), as listed in Table 3. Spectrum E_{abs} are

457 calculated from 370 to 950 nm as shown in Figure S11. E_{abs} in the PRD exhibits a weak wavelength

458 dependence, with slightly higher E_{abs} at the shorter wavelength (e.g. $E_{abs370} = 1.55\pm0.48$) and is

459 relatively lower in the IR range (e.g. $E_{abs950} = 1.49\pm0.49$).

4.2 Monthly characteristics of MAE, AAE and SSA

461 Monthly variations of MAE_{550} at the NC site are shown in Figure 6a and Table S2, revealing distinct

462 patterns of higher MAE_{550} in summer and lower in winter. On the other hand, $AAE_{470-660}$ is lower in

463 summer and higher in winter (Figure 6b and Table S3). Monthly SSA_{525} varied from 0.83 to 0.90

464 without a clear seasonal pattern, as shown in Figure S12 and Table S4. $MAE_{p,550}$ estimation for

465 individual months is shown in Figure 6a (the purple line) and monthly E_{abs550} is calculated accordingly

466 following Eq. 3 (Figure 6c). E_{abs550} shows clear seasonal variations, with higher values from April to

467 August (1.52~1.97 as shown in Table S5) and relatively lower values from September to March

468   (1.24~1.49). The highest enhancement is found in August (1.97). Factors affecting variation of E_{abs550}

469   are discussed in the following sections, including air mass origin, biomass burning and RH.

4.3 The effect of air mass origin

471   It's of interest to understand the seasonal variations of optical properties in the PRD. Hourly backward

472   trajectories for the past 72 hours were calculated using NOAA's HYSPLIT (Hybrid Single Particle

473   Lagrangian Integrated Trajectory, version 4) model (Draxier and Hess, 1998) from Feb 2012 to Jan

474   2013 as shown in Figure S13. Cluster analysis was conducted using MeteoInfo (Wang, 2014). By

475   examining the total spatial variance (TSV), the number of clusters was determined to be four as shown

476   in Figure S14. Cluster 1 (C1) represents continental air masses from the north, accounting for 44.4%

477   of total trajectories. C2 (22.8%) represents marine air masses coming from the South China Sea. C3

478   represents air masses from the east (Taiwan island). C4 (15.8%) represents transitional air masses

479   coming from the east coastline of China. As shown in Figure 7, E_{abs550} from C2 (1.78) is higher than

480   other clusters (1.30 – 1.42). Further Wilcoxon-Mann-Whitney tests show that E_{abs550} from C2 is

481   significantly higher than E_{abs550} from C1, C3 and C4 (Figure S15), implying that particles from the

482   South China Sea cluster is likely more aged than other clusters. Air mass origin in the PRD is

483   dominated by C2 from Apr to Aug (Figure S16a) as a result of the South China Sea monsoon in the

484   rainy season. In contrast, the dry season is ruled by continental air masses from the north (C1) due to

485   the influence of the northeast monsoon. E_{abs550} from C2 varied from 1.67 to 2.19, but was always

486   higher than E_{abs550} from C1 and C3 during the rainy season (Figure S16b). As a result, the domination

487   of aged air mass from the vast ocean is one of the reasons for the much higher E_{abs550} found in the rainy

488   season.

4.4 The effect of biomass burning

490   Biomass burning (BB) and vehicular emission are the two major sources of soot particles. BC

491   from biomass burning emission, depending on the fuel type and burning condition, may have a higher

492   OC/EC ratio and a thicker coating, resulting in a higher MAE than vehicular emission (Shen et al.,

493   2013; Cheng et al., 2016) . In this study, the influence of BB on optical properties is investigated using

494 the K^+/EC ratio as a BB indicator. As shown in Figure 8, MAE_{550} is positively correlated with the

495 K^+/EC ratio, which exhibits a clear seasonal pattern that is higher in the rainy season and lower in the

496 dry season (Figure S17a). Southeast Asia has the highest fire emission density globally due to the high

497 biofuel consumption along with frequent fire activity in this region (Aouizerats et al., 2015), making

498 Southeast Asia a large contributor to BC emissions (Jason Blake, 2014). During the rainy season when

499 oceanic wind prevails, BC from BB emission in Southeast Asia can reach PRD through long range

500 transport (LRT), resulting in an elevated K^+/EC ratio and MAE_{550}. The Deming regression intercept

501 (11.89) in Figure 8 represents the MAE without the BB effect. This non-BB MAE_{550} (11.89 $m^2\,g^{-1}$) is

502 only slightly lower than $MAE_{p,550}$ (13 $m^2\,g^{-1}$) obtained in section 4.3, implying that a large fraction of

503 $MAE_{p,550}$ could not be explained by the BB source. Additional evidence was obtained through

504 examining regression relationships of $MAE_{p,550}$ with K^+/EC month-by-month (Figure S17b).

505 Correlation of monthly $MAE_{p,550}$ vs. K^+/EC ratio yield a R^2 of 0.23 (Figure S17c). In contrast, a much

506 higher correlation (R^2=0.58) was observed (Figure S17d) between $MAE_{p,550}$ and non-BB MAE_{550} (i.e.,

507 K^+/EC intercepts from Figure S17b). These results imply that BB is one of the contributors to the

508 $MAE_{p,550}$ variations, but unlikely the dominating one.

509   Many studies have found that BB influenced samples exhibit elevated AAE due to the presence

510 of wavelength dependent light absorbing substances like BrC and HUmic-LIke Substances (HULIS)

511 (Kirchstetter et al., 2004; Hoffer et al., 2006; Sandradewi et al., 2008; Herich et al., 2011; Pokhrel et

512 al., 2017). It is of interest to investigate whether elevated AAE observed in the PRD during the dry

513 season is associated with BB influence. As shown in Figure S18, $AAE_{370-470}$ and $AAE_{470-660}$ did not

514 correlate with the BB indicator, K^+/EC ratio. These results suggest that the elevated AAE observed in

515 the PRD wintertime is unlikely to be dominated by the BB effect. Beside the independency between

516 $AAE_{470-660}$ and K^+/EC ratio, the measured $AAE_{470-660}$ range also implies that BB is not the major

517 driving force of $AAE_{470-660}$ variations. The limited light absorption contribution from BrC in RPD

518 region is observed in a recent study (Yuan et al., 2016) , which suggest an upper limit of BrC

519 contribution of 10% at 405 nm in the winter time using the AAE approach. As discussed in our Mie

520 simulation (section 3.1) and a previous study (Lack and Cappa, 2010), coating of non-absorbing

521 materials onto soot particles can increase AAE up to 2. Since the monthly average $AAE_{470-660}$ in

522   wintertime did not exceed 1.2 (Table S3), the variations of $AAE_{470-660}$ in the PRD are more likely

523   associated with coatings rather than the contribution of BrC. The results also imply that attempts on

524   BrC absorption attribution for the PRD dataset presented in this study could be risky, considering that

525   elevation of AAE is actually dominated by coating (Lack and Langridge, 2013).

526   4.5 The effect of relative humidity (RH) on optical properties

527   Soot particles are relatively hydrophobic when freshly emitted, but tend to gain hygroscopicity

528   during atmospheric aging. Hygroscopic growth of coated laboratory generated model BC was reported

529   by McMeeking et al. (2011). Growth of ambient BC particle size by a factor of 1.4-1.6 under high RH

530   has been observed in a UK study (Liu et al., 2013). Located in the subtropical zone, RH plays an

531   important role on aerosol optical properties in the PRD region. The yearlong measurements at the NC

532   site provide a unique opportunity to investigate the effect of RH on aerosol optical properties, since

533   most existing ad hoc studies in the PRD only last for months. Liquid water content (LWC) was

534   calculated using the E-AIM (model 2) thermodynamic model (Clegg et al., 1998). As shown in Figure

535   S19, LWC on average accounted for a significant fraction (44%) of non-EC $PM_{2.5}$ mass, making it an

536   important component of $PM_{2.5}$ mass and due to high RH in the PRD. Previously, hygroscopic growth

537   was only considered for particle scattering in the IMPROVE formula for chemically resolved light

538   extinction budget studies. In this study f(RH) of MAE was obtained from yearlong measurements as

539   shown in Figure 9a for RH = 30 ~100% and color coded for LWC. It clearly shows that MAE_{550}

540   measured in NC is positively correlated with RH and the enhancement can be fitted by a polynomial

541   equation. When RH is close to 100%, the LWC can account for 70% of $PM_{2.5}$ mass. The maximum

542   f(RH) can reach 1.3, which is higher than the value found in Beijing (1.2) (Wu et al., 2016b), but lower

543   than a numerical study (1.35) (Nessler et al., 2005). These results reveal that a large contribution of

544   E_{abs} is coming from high LWC under high RH in the PRD region. Because RH has a clear diurnal

545   pattern, it can affect the diurnal pattern of E_{abs} in the PRD. Since the RH effect on E_{abs} is rarely

546   considered in existing climate models, the inclusion of RH effect can reduce the uncertainty for

547   assessing BC's climate effect.

548   The $AAE_{470-660}$ dependency on RH is shown in Figure 9b. When RH is low (e.g. 30%), the

549    $AAE_{470-660}$ is around 1.25 and decreases to 1.10 as RH increases to 50%. $AAE_{470-660}$ remains around

550   1.12 when RH is 50-70%. Then $AAE_{470-660}$ decreases again when RH is higher than 70% and can reach

551   1 when RH is close to 100%. Since a higher RH results in hygroscopic growth and larger particle

552   diameters, the negative correlation between $AAE_{470-660}$ and RH provides a clue on soot particles'

553   primary diameter and mixing state. As shown in the Mie simulation in Figure 2b, for a particle with

554   D_{core} of 130 nm and D_{shell}/D_{core} of 2 to 4, $AAE_{470-660}$ decreases as the coating increases, and the decrease

555   tapers off when $D_{shell}/D_{core} = 3$. The D_{core} obtained here (130nm) is comparable with D_{core} obtained

556   from SP2 measurements (110nm) in the PRD (Huang et al., 2011a).

4.6 Implications for mixing state

558   Quantitative direct measurements of BC mixing state and coating thickness are still challenging.

559   SP2 can estimate the coating thickness using a lag-time approach or a Mie calculation approach can

560   be employed, but both methods have a limited range in coating thickness and uncertainties arise from

561   the assumptions made during the retrieval. For example, recent studies found that the mass equivalent

562   diameter of soot core measured by SP2 could be underestimated due to density assumptions (Zhang et

563   al., 2016b). Although size distribution measurement is not available in this study, clues of mixing state

564   still can be derived from bulk measurements of optical properties. As discussed in section 4.4.1,

565   elevated E_{abs550} observed in the rainy season is associated with aged air masses from a marine origin.

566   To probe the possible mixing state difference between dry and rainy season, E_{abs550}, SSA_{525} and

567    $AAE_{470-660}$ are used to narrow down the possible core-shell size range as shown in Figure S20. Monthly

568   averages with one standard deviation of $AAE_{470-660}$, SSA_{525} and E_{abs550} are used as constraints to extract

569   the intersecting core-shell size range from Figure 2a, Figure S4 and Figure 3a. January and August

570   data are used to represent two different scenarios: elevated $AAE_{470-660}$ (1.19±0.11) with lower E_{abs550}

571   (1.31±0.32) in dry season and low $AAE_{470-660}$ (1.04±0.09) with elevated E_{abs550} (1.97±0.71) in rainy

572   season. The results show that January and August have a very different core-shell size range: in

573   January, the core and shell range are 100 ~ 160 nm and 120 ~ 250 nm, respectively; in August, the

574 core and shell range are 120 ~ 165 nm and 170 ~ 430 nm, respectively. This confirms again that the

575 soot particles in the rainy season are likely to have a thicker coating than in the dry season.

5 Caveats of the MRS method in its applications to ambient data

577 The data in this study is dominated by BC absorption that did not show much influence from

578 BrC. However, extra care should be taken if the samples exhibit substantial BrC signature (e.g.

579 AAE>2). Such situations are equivalent to the two-source scenarios discussed in our previous paper

580 on the MRS method (Wu and Yu, 2016) and the major findings are described below. Two types of

581 two-source scenarios are considered: two correlated primary sources (scenario A) and two independent

582 primary sources (scenario B). In scenario A in which both BC and primary BrC are dominated by BB,

583 using BC as a solo tracer to calculate the primary ratio (MAE_p) still works. In scenario B in which BC

584 and primary BrC are independent, using BC alone to determine a single primary MAE_p could lead to

585 a considerable bias in E_{abs} estimation. Alternatively, if a reliable primary BrC tracer is available, the

586 corresponding $MAE_{p,BrC}$ can be determined by MRS. With the knowledge of $MAE_{p,BrC}$ and $MAE_{p,BC}$, light

587 absorption by BC and BrC can be calculated separately and the E_{abs} can be determined using Eq. (11) :

588 $$E_{abs} = \frac{\sigma_{abs,t}}{\sigma_{abs,p,BC} + \sigma_{abs,p,BrC}} = \frac{\sigma_{abs,t}}{MAE_{p,BC} \times EC + MAE_{p,BrC} \times BrC} \tag{11}$$

589 However, the implementation of Eq.11 is challenging due to the complexity in the chemical

590 composition of BrC. For example, a recent study found that the 20 most absorbing BrC chromophores

591 account for ~50% BrC light absorption and there is not a single compound contributing more than 10%

592 (Lin et al., 2016), making it difficult to choose a single compound as the BrC tracer. In addition, time

593 resolved measurement of BrC chromophores has yet to emerge. As a result, for scenario B (sample

594 AAE>2 & primary BrC variations independent of BC), estimation of E_{abs} by MRS is not practical at

595 this stage due to the lack of required input data. Using BC alone to determine a single primary MAE_p

596 could lead to a considerable bias and should be avoided.

6 Conclusions

In this study, a novel statistical approach is proposed and its application on ambient data is demonstrated using one-year hourly OC and EC data coupled with Aethalometer measurements. Unlike conventional E_{abs} determination approaches that require expensive instrumentation (e.g. TD-PAS, VTDMA, SP2), this new approach employs widely deployed instruments (field carbon analyzer and Aethalometer). The key of this new approach involves calculating MAE_p by the Minimum R Squared (MRS) method (Wu and Yu, 2016). It is found that E_{abs} estimation by MRS is insensitive to systematic biases in EC and σ_{abs} measurements. The annual average $MAE_{p,550}$ estimated by MRS is 13 $m^2 g^{-1}$ and annual average MAE_{550} is 18.75±6.16 $m^2 g^{-1}$, suggesting an annual average enhancement factor (E_{abs550}) of 1.50±0.48. This value is within the upper limit of E_{abs} (~2) by core-shell Mie simulations considering the typical soot size distribution and coating thickness in the PRD.

Both $MAE_{p,550}$ and E_{abs} show distinct seasonal variations, implying the complexity of soot particle mixing state variations in this region. The elevated summertime E_{abs550} in the PRD is found to be associated with the domination of aged air masses from the South China Sea, along with the long-range transport of biomass burning influenced air masses from Southeast Asia. Hygroscopic growth with elevated RH contributes to E_{abs} as well, which could be as high as 1.3. A negative correlation is found between $AAE_{470-660}$ and RH, suggesting a dominant particle size with a D_{core} of 130 nm and D_{shell}/D_{core} range of 2 to 4. Core-shell size ranges narrowed down by E_{abs550} and $AAE_{470-660}$ constraints suggest that soot particles in the rainy season are likely to have thicker coatings than in the dry season.

Data availability

OC, EC, inorganic ions and σ_{abs} data used in this study are available from corresponding authors upon request.

Acknowledgements
This work is supported by the National Natural Science Foundation of China (41605002, 41475004). We gratefully acknowledge the Fok Ying Tung Foundation for funding to the Atmospheric Research

623   Center at HKUST Fok Ying Tung Graduate School. The authors thank Jingxiang Huang of Fok Ying

624   Tung Graduate School for the assistance in OCEC analyzer maintenance. The authors are also grateful

625   to Dr. Stephen M Griffith and Dr. Yongjie Li for the helpful comments. The authors gratefully

626   acknowledge the NOAA Air Resources Laboratory (ARL) for the provision of the HYSPLIT transport

627   and dispersion model used in this publication.

References

Adler, G., Riziq, A. A., Erlick, C., and Rudich, Y.: Effect of intrinsic organic carbon on the optical properties of fresh diesel soot, Proceedings of the National Academy of Sciences, 107, 6699-6704, doi: 10.1073/pnas.0903311106, 2010.

Ajtai, T., Filep, Á., Utry, N., Schnaiter, M., Linke, C., Bozóki, Z., Szabó, G., and Leisner, T.: Inter-comparison of optical absorption coefficients of atmospheric aerosols determined by a multi-wavelength photoacoustic spectrometer and an Aethalometer under sub-urban wintry conditions, J. Aerosol. Sci., 42, 859-866, doi: 10.1016/j.jaerosci.2011.07.008, 2011.

Alexander, D. T. L., Crozier, P. A., and Anderson, J. R.: Brown carbon spheres in East Asian outflow and their optical properties, Science, 321, 833-836, 2008.

Andreae, M. O., Schmid, O., Yang, H., Chand, D., Yu, J. Z., Zeng, L. M., and Zhang, Y. H.: Optical properties and chemical composition of the atmospheric aerosol in urban Guangzhou, China, Atmos. Environ., 42, 6335-6350, doi: 10.1016/j.atmosenv.2008.01.030, 2008.

Aouizerats, B., van der Werf, G. R., Balasubramanian, R., and Betha, R.: Importance of transboundary transport of biomass burning emissions to regional air quality in Southeast Asia during a high fire event, Atmos. Chem. Phys., 15, 363-373, doi: 10.5194/acp-15-363-2015, 2015.

Arnott, W. P., Moosmuller, H., Sheridan, P. J., Ogren, J. A., Raspet, R., Slaton, W. V., Hand, J. L., Kreidenweis, S. M., and Collett, J. L.: Photoacoustic and filter-based ambient aerosol light absorption measurements: Instrument comparisons and the role of relative humidity, J. Geophys. Res., 108, 2003.

Arnott, W. P., Hamasha, K., Moosmuller, H., Sheridan, P. J., and Ogren, J. A.: Towards aerosol light-absorption measurements with a 7-wavelength Aethalometer: Evaluation with a photoacoustic instrument and 3-wavelength nephelometer, Aerosol. Sci. Technol., 39, 17-29, doi: Doi 10.1080/027868290901972, 2005.

Bauer, J. J., Yu, X.-Y., Cary, R., Laulainen, N., and Berkowitz, C.: Characterization of the sunset semi-continuous carbon aerosol analyzer, J. Air Waste Manage. Assoc., 59, 826-833, doi: 10.3155/1047-3289.59.7.826, 2009.

Bohren, C. F. and Huffman, D. R.: Absorption and scattering of light by small particles, Wiley, New York, xiv, 530 p. pp., 1983.

Bond, T. C.: Spectral dependence of visible light absorption by carbonaceous particles emitted from coal combustion, Geophys. Res. Lett., 28, 4075-4078, doi: Doi 10.1029/2001gl013652, 2001.

Bond, T. C. and Bergstrom, R. W.: Light absorption by carbonaceous particles: An investigative review, Aerosol. Sci. Technol., 40, 27-67, doi: Doi 10.1080/02786820500421521, 2006.

Bond, T. C., Habib, G., and Bergstrom, R. W.: Limitations in the enhancement of visible light absorption due to mixing state, J. Geophys. Res., 111, -, 2006.

Bond, T. C., Zarzycki, C., Flanner, M. G., and Koch, D. M.: Quantifying immediate radiative forcing by black carbon and organic matter with the Specific Forcing Pulse, Atmos. Chem. Phys., 11, 1505-1525, doi: 10.5194/acp-11-1505-2011, 2011.

Cappa, C. D., Lack, D. A., Burkholder, J. B., and Ravishankara, A. R.: Bias in Filter-Based Aerosol Light Absorption Measurements Due to Organic Aerosol Loading: Evidence from Laboratory Measurements, Aerosol. Sci. Technol., 42, 1022-1032, doi: 10.1080/02786820802389285, 2008.

669   Cappa, C. D., Onasch, T. B., Massoli, P., Worsnop, D. R., Bates, T. S., Cross, E. S., Davidovits, P.,
670   Hakala, J., Hayden, K. L., Jobson, B. T., Kolesar, K. R., Lack, D. A., Lerner, B. M., Li, S.-M., Mellon,
671   D., Nuaaman, I., Olfert, J. S., Petäjä, T., Quinn, P. K., Song, C., Subramanian, R., Williams, E. J., and
672   Zaveri, R. A.: Radiative Absorption Enhancements Due to the Mixing State of Atmospheric Black
673   Carbon, Science, 337, 1078-1081, doi: 10.1126/science.1223447, 2012.

674   Chan, T. W., Brook, J. R., Smallwood, G. J., and Lu, G.: Time-resolved measurements of black carbon
675   light absorption enhancement in urban and near-urban locations of southern Ontario, Canada, Atmos.
676   Chem. Phys., 11, 10407-10432, 2011.

677   Chen, B., Bai, Z., Cui, X., Chen, J., Andersson, A., and Gustafsson, Ö.: Light absorption enhancement
678   of black carbon from urban haze in Northern China winter, Environ Pollut, 221, 418-426, doi:
679   10.1016/j.envpol.2016.12.004, 2017.

680   Cheng, Y., Engling, G., Moosmüller, H., Arnott, W. P., Chen, L. W. A., Wold, C. E., Hao, W. M., and
681   He, K.-b.: Light absorption by biomass burning source emissions, Atmos. Environ., 127, 347-354, doi:
682   10.1016/j.atmosenv.2015.12.045, 2016.

683   China, S., Mazzoleni, C., Gorkowski, K., Aiken, A. C., and Dubey, M. K.: Morphology and mixing
684   state of individual freshly emitted wildfire carbonaceous particles, Nat Commun, 4, doi:
685   10.1038/ncomms3122, 2013.

686   Chow, J. C., Watson, J. G., Doraiswamy, P., Chen, L. W. A., Sodeman, D. A., Lowenthal, D. H., Park,
687   K., Arnott, W. P., and Motallebi, N.: Aerosol light absorption, black carbon, and elemental carbon at
688   the Fresno Supersite, California, Atmos Res, 93, 874-887, doi: DOI 10.1016/j.atmosres.2009.04.010,
689   2009.

690   Clegg, S. L., Brimblecombe, P., and Wexler, A. S.: Thermodynamic Model of the System
691   H+−NH4+−SO42-−NO3-−H2O at Tropospheric Temperatures, The Journal of Physical Chemistry A,
692   102, 2137-2154, doi: 10.1021/jp973042r, 1998.

693   Coen, M. C., Weingartner, E., Apituley, A., Ceburnis, D., Fierz-Schmidhauser, R., Flentje, H.,
694   Henzing, J. S., Jennings, S. G., Moerman, M., Petzold, A., Schmid, O., and Baltensperger, U.:
695   Minimizing light absorption measurement artifacts of the Aethalometer: evaluation of five correction
696   algorithms, Atmos. Meas. Tech., 3, 457-474, doi: 10.5194/amt-3-457-2010, 2010.

697   Cui, F., Chen, M., Ma, Y., Zheng, J., Zhou, Y., Li, S., Qi, L., and Wang, L.: An intensive study on
698   aerosol optical properties and affecting factors in Nanjing, China, Journal of Environmental Sciences,
699   40, 35-43, doi: 10.1016/j.jes.2015.08.017, 2016a.

700   Cui, X., Wang, X., Yang, L., Chen, B., Chen, J., Andersson, A., and Gustafsson, Ö.: Radiative
701   absorption enhancement from coatings on black carbon aerosols, Sci.Total.Environ., 551, 51-56, doi:
702   10.1016/j.scitotenv.2016.02.026, 2016b.

703   Dastanpour, R., Momenimovahed, A., Thomson, K., Olfert, J., and Rogak, S.: Variation of the optical
704   properties of soot as a function of particle mass, Carbon, 124, 201-211, doi:
705   10.1016/j.carbon.2017.07.005, 2017.

706   Ding, A. J., Huang, X., Nie, W., Sun, J. N., Kerminen, V. M., Petäjä, T., Su, H., Cheng, Y. F., Yang,
707   X. Q., Wang, M. H., Chi, X. G., Wang, J. P., Virkkula, A., Guo, W. D., Yuan, J., Wang, S. Y., Zhang,
708   R. J., Wu, Y. F., Song, Y., Zhu, T., Zilitinkevich, S., Kulmala, M., and Fu, C. B.: Enhanced haze
709   pollution by black carbon in megacities in China, Geophys. Res. Lett., 43, 2873-2879, doi:
710   10.1002/2016GL067745, 2016.

711 Doran, J. C., Barnard, J. C., Arnott, W. P., Cary, R., Coulter, R., Fast, J. D., Kassianov, E. I., Kleinman,
712 L., Laulainen, N. S., Martin, T., Paredes-Miranda, G., Pekour, M. S., Shaw, W. J., Smith, D. F.,
713 Springston, S. R., and Yu, X. Y.: The T1-T2 study: evolution of aerosol properties downwind of
714 Mexico City, Atmos. Chem. Phys., 7, 1585-1598, doi: 10.5194/acp-7-1585-2007, 2007.
715 Draxier, R. R. and Hess, G. D.: An overview of the HYSPLIT_4 modelling system for trajectories,
716 dispersion and deposition, Aust Meteorol Mag, 47, 295-308, 1998.
717 Drinovec, L., Gregorič, A., Zotter, P., Wolf, R., Bruns, E. A., Prévôt, A. S. H., Petit, J. E., Favez, O.,
718 Sciare, J., Arnold, I. J., Chakrabarty, R. K., Moosmüller, H., Filep, A., and Močnik, G.: The filter-
719 loading effect by ambient aerosols in filter absorption photometers depends on the coating of the
720 sampled particles, Atmos. Meas. Tech., 10, 1043-1059, doi: 10.5194/amt-10-1043-2017, 2017.
721 Fuller, K. A., Malm, W. C., and Kreidenweis, S. M.: Effects of mixing on extinction by carbonaceous
722 particles, J. Geophys. Res., 104, 15941-15954, 1999.
723 Gong, X., Zhang, C., Chen, H., Nizkorodov, S. A., Chen, J., and Yang, X.: Size distribution and mixing
724 state of black carbon particles during a heavy air pollution episode in Shanghai, Atmos. Chem. Phys.,
725 16, 5399-5411, doi: 10.5194/acp-16-5399-2016, 2016.
726 Guo, S., Hu, M., Lin, Y., Gomez-Hernandez, M., Zamora, M. L., Peng, J., Collins, D. R., and Zhang,
727 R.: OH-Initiated Oxidation of m-Xylene on Black Carbon Aging, Environ. Sci. Technol., doi:
728 10.1021/acs.est.6b01272, 2016.
729 Guyon, P., Graham, B., Roberts, G. C., Mayol-Bracero, O. L., Maenhaut, W., Artaxo, P., and Andreae,
730 M. O.: Sources of optically active aerosol particles over the Amazon forest, Atmos. Environ., 38, 1039-
731 1051, doi: 10.1016/j.atmosenv.2003.10.051, 2004.
732 Hansen, A. D. A.: The Aethalometer Manual, Berkeley, California,USA, Magee Scientific, 2005.
733 Hansen, J. and Nazarenko, L.: Soot climate forcing via snow and ice albedos, P Natl Acad Sci USA,
734 101, 423-428, doi: DOI 10.1073/pnas.2237157100, 2004.
735 Herich, H., Hueglin, C., and Buchmann, B.: A 2.5 year's source apportionment study of black carbon
736 from wood burning and fossil fuel combustion at urban and rural sites in Switzerland, Atmos. Meas.
737 Tech., 4, 1409-1420, doi: DOI 10.5194/amt-4-1409-2011, 2011.
738 Hoffer, A., Gelencser, A., Guyon, P., Kiss, G., Schmid, O., Frank, G. P., Artaxo, P., and Andreae, M.
739 O.: Optical properties of humic-like substances (HULIS) in biomass-burning aerosols, Atmos. Chem.
740 Phys., 6, 3563-3570, 2006.
741 Huang, X. F., Gao, R. S., Schwarz, J. P., He, L. Y., Fahey, D. W., Watts, L. A., McComiskey, A.,
742 Cooper, O. R., Sun, T. L., Zeng, L. W., Hu, M., and Zhang, Y. H.: Black carbon measurements in the
743 Pearl River Delta region of China, J. Geophys. Res., 116, D12208, doi: 10.1029/2010jd014933, 2011a.
744 Huang, X. F., He, L. Y., Hu, M., Canagaratna, M. R., Kroll, J. H., Ng, N. L., Zhang, Y. H., Lin, Y.,
745 Xue, L., Sun, T. L., Liu, X. G., Shao, M., Jayne, J. T., and Worsnop, D. R.: Characterization of
746 submicron aerosols at a rural site in Pearl River Delta of China using an Aerodyne High-Resolution
747 Aerosol Mass Spectrometer, Atmos. Chem. Phys., 11, 1865-1877, doi: 10.5194/acp-11-1865-2011,
748 2011b.
749 IPCC: Climate change 2013 : the physical science basis : Working Group I contribution to the Fifth
750 Assessment Report of the Intergovernmental Panel on Climate Change, xi, 1535 pages. pp., 2013.
751 Jacobson, M. Z.: Effects of externally-through-internally-mixed soot inclusions within clouds and
752 precipitation on global climate, J Phys Chem A, 110, 6860-6873, 2006.

753   Jason Blake, C.: Quantifying the occurrence and magnitude of the Southeast Asian fire climatology,

754   Environmental Research Letters, 9, 114018, 2014.

755   Jung, J., Lee, H., Kim, Y. J., Liu, X., Zhang, Y., Gu, J., and Fan, S.: Aerosol chemistry and the effect

756   of aerosol water content on visibility impairment and radiative forcing in Guangzhou during the 2006

757   Pearl River Delta campaign, Journal of Environmental Management, 90, 3231-3244, doi:

758   10.1016/j.jenvman.2009.04.021, 2009.

759   Khalizov, A. F., Xue, H. X., Wang, L., Zheng, J., and Zhang, R. Y.: Enhanced Light Absorption and

760   Scattering by Carbon Soot Aerosol Internally Mixed with Sulfuric Acid, J Phys Chem A, 113, 1066-

761   1074, 2009.

762   Kirchstetter, T. W., Novakov, T., and Hobbs, P. V.: Evidence that the spectral dependence of light

763   absorption by aerosols is affected by organic carbon, J. Geophys. Res., 109, D21208, doi:

764   10.1029/2004jd004999, 2004.

765   Knox, A., Evans, G. J., Brook, J. R., Yao, X., Jeong, C. H., Godri, K. J., Sabaliauskas, K., and Slowik,

766   J. G.: Mass Absorption Cross-Section of Ambient Black Carbon Aerosol in Relation to Chemical Age,

767   Aerosol. Sci. Technol., 43, 522-532, doi: Doi 10.1080/02786820902777207, 2009.

768   Koch, D. and Del Genio, A.: Black carbon semi-direct effects on cloud cover: review and synthesis,

769   Atmos. Chem. Phys., 10, 7685-7696, 2010.

770   Kozlov, V. S., Panchenko, M. V., Tikhomirov, A. B., Tikhomirov, B. A., and Shmargunov, V. P.:

771   Effect of relative air humidity on photoacoustic aerosol absorption measurements in the near-ground

772   atmospheric layer, Atmospheric and Oceanic Optics, 24, 487, doi: 10.1134/s1024856011050101, 2011.

773   Laborde, M., Mertes, P., Zieger, P., Dommen, J., Baltensperger, U., and Gysel, M.: Sensitivity of the

774   Single Particle Soot Photometer to different black carbon types, Atmos. Meas. Tech., 5, 1031-1043,

775   2012.

776   Lack, D. A. and Cappa, C. D.: Impact of brown and clear carbon on light absorption enhancement,

777   single scatter albedo and absorption wavelength dependence of black carbon, Atmos. Chem. Phys., 10,

778   4207-4220, doi: DOI 10.5194/acp-10-4207-2010, 2010.

779   Lack, D. A., Langridge, J. M., Bahreini, R., Cappa, C. D., Middlebrook, A. M., and Schwarz, J. P.:

780   Brown carbon and internal mixing in biomass burning particles, P Natl Acad Sci USA, 109, 14802-

781   14807, doi: 10.1073/pnas.1206575109, 2012a.

782   Lack, D. A., Richardson, M. S., Law, D., Langridge, J. M., Cappa, C. D., McLaughlin, R. J., and

783   Murphy, D. M.: Aircraft instrument for comprehensive characterization of aerosol optical properties,

784   Part 2: black and brown carbon absorption and absorption enhancement measured with photo acoustic

785   spectroscopy, Aerosol. Sci. Technol., 46, 555-568, 2012b.

786   Lack, D. A. and Langridge, J. M.: On the attribution of black and brown carbon light absorption using

787   the Ångström exponent, Atmos. Chem. Phys., 13, 10535-10543, doi: 10.5194/acp-13-10535-2013,

788   2013.

789   Lan, Z.-J., Huang, X.-F., Yu, K.-Y., Sun, T.-L., Zeng, L.-W., and Hu, M.: Light absorption of black

790   carbon aerosol and its enhancement by mixing state in an urban atmosphere in South China, Atmos.

791   Environ., 69, 118-123, doi: 10.1016/j.atmosenv.2012.12.009, 2013.

792   Langridge, J. M., Richardson, M. S., Lack, D. A., Brock, C. A., and Murphy, D. M.: Limitations of

793   the Photoacoustic Technique for Aerosol Absorption Measurement at High Relative Humidity,

794   Aerosol. Sci. Technol., 47, 1163-1173, doi: 10.1080/02786826.2013.827324, 2013.

795 Leung, K. K., Schnitzler, E. G., Jäger, W., and Olfert, J. S.: Relative Humidity Dependence of Soot
796 Aggregate Restructuring Induced by Secondary Organic Aerosol: Effects of Water on Coating
797 Viscosity and Surface Tension, Environmental Science & Technology Letters, doi:
798 10.1021/acs.estlett.7b00298, 2017.

799 Lewis, K. A., Arnott, W. P., Moosmuller, H., Chakrabarty, R. K., Carrico, C. M., Kreidenweis, S. M.,
800 Day, D. E., Malm, W. C., Laskin, A., Jimenez, J. L., Ulbrich, I. M., Huffman, J. A., Onasch, T. B.,
801 Trimborn, A., Liu, L., and Mishchenko, M. I.: Reduction in biomass burning aerosol light absorption
802 upon humidification: roles of inorganically-induced hygroscopicity, particle collapse, and
803 photoacoustic heat and mass transfer, Atmos. Chem. Phys., 9, 8949-8966, 2009a.

804 Lewis, K. A., Arnott, W. P., Moosmüller, H., Chakrabarty, R. K., Carrico, C. M., Kreidenweis, S. M.,
805 Day, D. E., Malm, W. C., Laskin, A., Jimenez, J. L., Ulbrich, I. M., Huffman, J. A., Onasch, T. B.,
806 Trimborn, A., Liu, L., and Mishchenko, M. I.: Reduction in biomass burning aerosol light absorption
807 upon humidification: roles of inorganically-induced hygroscopicity, particle collapse, and
808 photoacoustic heat and mass transfer, Atmos. Chem. Phys., 9, 8949-8966, doi: 10.5194/acp-9-8949-
809 2009, 2009b.

810 Lin, P., Aiona, P. K., Li, Y., Shiraiwa, M., Laskin, J., Nizkorodov, S. A., and Laskin, A.: Molecular
811 Characterization of Brown Carbon in Biomass Burning Aerosol Particles, Environ. Sci. Technol., 50,
812 11815-11824, doi: 10.1021/acs.est.6b03024, 2016.

813 Liu, D., Allan, J., Whitehead, J., Young, D., Flynn, M., Coe, H., McFiggans, G., Fleming, Z. L., and
814 Bandy, B.: Ambient black carbon particle hygroscopic properties controlled by mixing state and
815 composition, Atmos. Chem. Phys., 13, 2015-2029, doi: 10.5194/acp-13-2015-2013, 2013.

816 Liu, D., Whitehead, J., Alfarra, M. R., Reyes-Villegas, E., Spracklen, D. V., Reddington, C. L., Kong,
817 S., Williams, P. I., Ting, Y.-C., Haslett, S., Taylor, J. W., Flynn, M. J., Morgan, W. T., McFiggans, G.,
818 Coe, H., and Allan, J. D.: Black-carbon absorption enhancement in the atmosphere determined by
819 particle mixing state, Nature Geosci, 10, 184-188, doi: 10.1038/ngeo2901, 2017.

820 Liu, F., Yon, J., and Bescond, A.: On the radiative properties of soot aggregates – Part 2: Effects of
821 coating, Journal of Quantitative Spectroscopy and Radiative Transfer, 172, 134-145, doi:
822 10.1016/j.jqsrt.2015.08.005, 2016a.

823 Liu, J., Lin, P., Laskin, A., Laskin, J., Kathmann, S. M., Wise, M., Caylor, R., Imholt, F., Selimovic,
824 V., and Shilling, J. E.: Optical properties and aging of light-absorbing secondary organic aerosol,
825 Atmos. Chem. Phys., 16, 12815-12827, doi: 10.5194/acp-16-12815-2016, 2016b.

826 Liu, S., Aiken, A. C., Gorkowski, K., Dubey, M. K., Cappa, C. D., Williams, L. R., Herndon, S. C.,
827 Massoli, P., Fortner, E. C., Chhabra, P. S., Brooks, W. A., Onasch, T. B., Jayne, J. T., Worsnop, D. R.,
828 China, S., Sharma, N., Mazzoleni, C., Xu, L., Ng, N. L., Liu, D., Allan, J. D., Lee, J. D., Fleming, Z.
829 L., Mohr, C., Zotter, P., Szidat, S., and Prevot, A. S. H.: Enhanced light absorption by mixed source
830 black and brown carbon particles in UK winter, Nat Commun, 6, doi: 10.1038/ncomms9435, 2015.

831 Ma, N., Zhao, C. S., Muller, T., Cheng, Y. F., Liu, P. F., Deng, Z. Z., Xu, W. Y., Ran, L., Nekat, B.,
832 van Pinxteren, D., Gnauk, T., Mueller, K., Herrmann, H., Yan, P., Zhou, X. J., and Wiedensohler, A.:
833 A new method to determine the mixing state of light absorbing carbonaceous using the measured
834 aerosol optical properties and number size distributions, Atmos. Chem. Phys., 12, 2381-2397, doi:
835 DOI 10.5194/acp-12-2381-2012, 2012.

836 Replacement Filter Tape for the Magee Scientific Model AE33 Aethalometer®:
837 http://www.mageesci.com/images/stories/docs/Magee_Scientific_Filter_Aethalometer_AE_Tape_Re
838 placement_discussion.pdf, 2017.

839 Matsui, H., Koike, M., Kondo, Y., Moteki, N., Fast, J. D., and Zaveri, R. A.: Development and
840 validation of a black carbon mixing state resolved three-dimensional model: Aging processes and
841 radiative impact, J. Geophys. Res., 118, 2304-2326, doi: 10.1029/2012JD018446, 2013.

842 McMeeking, G. R., Good, N., Petters, M. D., McFiggans, G., and Coe, H.: Influences on the fraction
843 of hydrophobic and hydrophilic black carbon in the atmosphere, Atmos. Chem. Phys., 11, 5099-5112,
844 doi: 10.5194/acp-11-5099-2011, 2011.

845 McMeeking, G. R., Fortner, E., Onasch, T. B., Taylor, J. W., Flynn, M., Coe, H., and Kreidenweis, S.
846 M.: Impacts of nonrefractory material on light absorption by aerosols emitted from biomass burning,
847 J. Geophys. Res., 119, 12,272-212,286, doi: 10.1002/2014JD021750, 2014.

848 Moffet, R. C., O'Brien, R. E., Alpert, P. A., Kelly, S. T., Pham, D. Q., Gilles, M. K., Knopf, D. A., and
849 Laskin, A.: Morphology and mixing of black carbon particles collected in central California during the
850 CARES field study, Atmos. Chem. Phys., 16, 14515-14525, doi: 10.5194/acp-16-14515-2016, 2016.

851 Moosmuller, H., Chakrabarty, R. K., Ehlers, K. M., and Arnott, W. P.: Absorption Angstrom
852 coefficient, brown carbon, and aerosols: basic concepts, bulk matter, and spherical particles, Atmos.
853 Chem. Phys., 11, 1217-1225, doi: DOI 10.5194/acp-11-1217-2011, 2011.

854 Moteki, N., Kondo, Y., and Adachi, K.: Identification by single-particle soot photometer of black
855 carbon particles attached to other particles: Laboratory experiments and ground observations in Tokyo,
856 J. Geophys. Res., 119, 2013JD020655, doi: 10.1002/2013jd020655, 2014.

857 Nakayama, T., Ikeda, Y., Sawada, Y., Setoguchi, Y., Ogawa, S., Kawana, K., Mochida, M., Ikemori,
858 F., Matsumoto, K., and Matsumi, Y.: Properties of light-absorbing aerosols in the Nagoya urban area,
859 Japan, in August 2011 and January 2012: Contributions of brown carbon and lensing effect, J. Geophys.
860 Res., 119, 2014JD021744, doi: 10.1002/2014JD021744, 2014.

861 Naoe, H., Hasegawa, S., Heintzenberg, J., Okada, K., Uchiyama, A., Zaizen, Y., Kobayashi, E., and
862 Yamazaki, A.: State of mixture of atmospheric submicrometer black carbon particles and its effect on
863 particulate light absorption, Atmos. Environ., 43, 1296-1301, doi: 10.1016/j.atmosenv.2008.11.031,
864 2009.

865 Nessler, R., Weingartner, E., and Baltensperger, U.: Effect of humidity on aerosol light absorption and
866 its implications for extinction and the single scattering albedo illustrated for a site in the lower free
867 troposphere, J. Aerosol. Sci., 36, 958-972, doi: 10.1016/j.jaerosci.2004.11.012, 2005.

868 Nordmann, S., Cheng, Y. F., Carmichael, G. R., Yu, M., Denier van der Gon, H. A. C., Zhang, Q.,
869 Saide, P. E., Pöschl, U., Su, H., Birmili, W., and Wiedensohler, A.: Atmospheric black carbon and
870 warming effects influenced by the source and absorption enhancement in central Europe, Atmos. Chem.
871 Phys., 14, 12683-12699, doi: 10.5194/acp-14-12683-2014, 2014.

872 Pandey, A., Pervez, S., and Chakrabarty, R. K.: Filter-based measurements of UV–vis mass absorption
873 cross sections of organic carbon aerosol from residential biomass combustion: Preliminary findings
874 and sources of uncertainty, Journal of Quantitative Spectroscopy and Radiative Transfer, 182, 296-
875 304, doi: 10.1016/j.jqsrt.2016.06.023, 2016.

876 Peng, J., Hu, M., Guo, S., Du, Z., Zheng, J., Shang, D., Levy Zamora, M., Zeng, L., Shao, M., Wu, Y.-
877 S., Zheng, J., Wang, Y., Glen, C. R., Collins, D. R., Molina, M. J., and Zhang, R.: Markedly enhanced

878   absorption and direct radiative forcing of black carbon under polluted urban environments,
879   Proceedings of the National Academy of Sciences, 113, 4266-4271, doi: 10.1073/pnas.1602310113,
880   2016.

881   Pokhrel, R. P., Beamesderfer, E. R., Wagner, N. L., Langridge, J. M., Lack, D. A., Jayarathne, T.,
882   Stone, E. A., Stockwell, C. E., Yokelson, R. J., and Murphy, S. M.: Relative importance of black
883   carbon, brown carbon, and absorption enhancement from clear coatings in biomass burning emissions,
884   Atmos. Chem. Phys., 17, 5063-5078, doi: 10.5194/acp-17-5063-2017, 2017.

885   Ramanathan, V. and Carmichael, G.: Global and regional climate changes due to black carbon, Nat
886   Geosci, 1, 221-227, doi: Doi 10.1038/Ngeo156, 2008.

887   Raspet, R., Slaton, W. V., Arnott, W. P., and Moosmüller, H.: Evaporation–Condensation Effects on
888   Resonant Photoacoustics of Volatile Aerosols, Journal of Atmospheric and Oceanic Technology, 20,
889   685-695, doi: 10.1175/1520-0426(2003)20<685:eceorp>2.0.co;2, 2003.

890   Reid, J. S., Eck, T. F., Christopher, S. A., Koppmann, R., Dubovik, O., Eleuterio, D. P., Holben, B. N.,
891   Reid, E. A., and Zhang, J.: A review of biomass burning emissions part III: intensive optical properties
892   of biomass burning particles, Atmos. Chem. Phys., 5, 827-849, doi: 10.5194/acp-5-827-2005, 2005.

893   Roden, C. A., Bond, T. C., Conway, S., and Pinel, A. B. O.: Emission factors and real-time optical
894   properties of particles emitted from traditional wood burning cookstoves, Environ. Sci. Technol., 40,
895   6750-6757, doi: 10.1021/es052080i, 2006.

896   Rose, D., Wehner, B., Ketzel, M., Engler, C., Voigtländer, J., Tuch, T., and Wiedensohler, A.:
897   Atmospheric number size distributions of soot particles and estimation of emission factors, Atmos.
898   Chem. Phys., 6, 1021-1031, doi: 10.5194/acp-6-1021-2006, 2006.

899   Saathoff, H., Naumann, K. H., Schnaiter, M., Schöck, W., Möhler, O., Schurath, U., Weingartner, E.,
900   Gysel, M., and Baltensperger, U.: Coating of soot and (NH4)2SO4 particles by ozonolysis products of
901   α-pinene, J. Aerosol. Sci., 34, 1297-1321, doi: 10.1016/S0021-8502(03)00364-1, 2003.

902   Sandradewi, J., Prévôt, A. S. H., Weingartner, E., Schmidhauser, R., Gysel, M., and Baltensperger, U.:
903   A study of wood burning and traffic aerosols in an Alpine valley using a multi-wavelength
904   Aethalometer, Atmos. Environ., 42, 101-112, doi: 10.1016/j.atmosenv.2007.09.034, 2008.

905   Saturno, J., Pöhlker, C., Massabò, D., Brito, J., Carbone, S., Cheng, Y., Chi, X., Ditas, F., Hrabě de
906   Angelis, I., Morán-Zuloaga, D., Pöhlker, M. L., Rizzo, L. V., Walter, D., Wang, Q., Artaxo, P., Prati,
907   P., and Andreae, M. O.: Comparison of different Aethalometer correction schemes and a reference
908   multi-wavelength absorption technique for ambient aerosol data, Atmos. Meas. Tech., 10, 2837-2850,
909   doi: 10.5194/amt-10-2837-2017, 2017.

910   Schmid, O., Artaxo, P., Arnott, W. P., Chand, D., Gatti, L. V., Frank, G. P., Hoffer, A., Schnaiter, M.,
911   and Andreae, M. O.: Spectral light absorption by ambient aerosols influenced by biomass burning in
912   the Amazon Basin. I: Comparison and field calibration of absorption measurement techniques, Atmos.
913   Chem. Phys., 6, 3443-3462, 2006.

914   Schnaiter, M., Linke, C., Mohler, O., Naumann, K. H., Saathoff, H., Wagner, R., Schurath, U., and
915   Wehner, B.: Absorption amplification of black carbon internally mixed with secondary organic aerosol,
916   J. Geophys. Res., 110, -, 2005.

917   Schwarz, J. P., Spackman, J. R., Fahey, D. W., Gao, R. S., Lohmann, U., Stier, P., Watts, L. A.,
918   Thomson, D. S., Lack, D. A., Pfister, L., Mahoney, M. J., Baumgardner, D., Wilson, J. C., and Reeves,

919   J. M.: Coatings and their enhancement of black carbon light absorption in the tropical atmosphere, J.
920   Geophys. Res., 113, -, 2008.

921   Sedlacek, A. J., Lewis, E. R., Kleinman, L., Xu, J. Z., and Zhang, Q.: Determination of and evidence
922   for non-core-shell structure of particles containing black carbon using the Single-Particle Soot
923   Photometer (SP2), Geophys. Res. Lett., 39, 2012.

924   Shen, G., Chen, Y., Wei, S., Fu, X., Zhu, Y., and Tao, S.: Mass absorption efficiency of elemental
925   carbon for source samples from residential biomass and coal combustions, Atmos. Environ., 79, 79-
926   84, doi: 10.1016/j.atmosenv.2013.05.082, 2013.

927   Shiraiwa, M., Kondo, Y., Iwamoto, T., and Kita, K.: Amplification of Light Absorption of Black
928   Carbon by Organic Coating, Aerosol. Sci. Technol., 44, 46-54, 2010.

929   Suglia, S. F., Gryparis, A., Wright, R. O., Schwartz, J., and Wright, R. J.: Association of Black Carbon
930   with Cognition among Children in a Prospective Birth Cohort Study, American Journal of
931   Epidemiology, 167, 280-286, doi: 10.1093/aje/kwm308, 2008.

932   Tan, H., Liu, L., Fan, S., Li, F., Yin, Y., Cai, M., and Chan, P. W.: Aerosol optical properties and
933   mixing state of black carbon in the Pearl River Delta, China, Atmos. Environ., 131, 196-208, doi:
934   10.1016/j.atmosenv.2016.02.003, 2016.

935   Tao, W. K., Chen, J. P., Li, Z. Q., Wang, C., and Zhang, C. D.: Impact of Aerosols on Convective
936   Clouds and Precipitation, Rev Geophys, 50, Rg2001, doi: Doi 10.1029/2011rg000369, 2012.

937   Tavakoli, F. and Olfert, J. S.: Determination of particle mass, effective density, mass–mobility
938   exponent, and dynamic shape factor using an aerodynamic aerosol classifier and a differential mobility
939   analyzer in tandem, J. Aerosol. Sci., 75, 35-42, doi: 10.1016/j.jaerosci.2014.04.010, 2014.

940   ten Brink, H., Otjes, R., Jongejan, P., and Slanina, S.: An instrument for semi-continuous monitoring
941   of the size-distribution of nitrate, ammonium, sulphate and chloride in aerosol, Atmos. Environ., 41,
942   2768-2779, doi: 10.1016/j.atmosenv.2006.11.041, 2007.

943   Turpin, B. J. and Huntzicker, J. J.: Secondary Formation of Organic Aerosol in the Los-Angeles Basin
944   - a Descriptive Analysis of Organic and Elemental Carbon Concentrations, Atmos. Environ., 25, 207-
945   215, 1991.

946   Ueda, S., Nakayama, T., Taketani, F., Adachi, K., Matsuki, A., Iwamoto, Y., Sadanaga, Y., and
947   Matsumi, Y.: Light absorption and morphological properties of soot-containing aerosols observed at
948   an East Asian outflow site, Noto Peninsula, Japan, Atmos. Chem. Phys., 16, 2525-2541, doi:
949   10.5194/acp-16-2525-2016, 2016.

950   Virkkula, A., Makela, T., Hillamo, R., Yli-Tuomi, T., Hirsikko, A., Hameri, K., and Koponen, I. K.:
951   A simple procedure for correcting loading effects of aethalometer data, J. Air Waste Manage. Assoc.,
952   57, 1214-1222, 2007.

953   Wang, Q., Huang, R., Zhao, Z., Cao, J., Ni, H., Tie, X., Zhu, C., Shen, Z., Wang, M., and Dai, W.:
954   Effects of photochemical oxidation on the mixing state and light absorption of black carbon in the
955   urban atmosphere of China, Environmental Research Letters, 12, 044012, 2017.

956   Wang, Q. Y., Huang, R. J., Cao, J. J., Han, Y. M., Wang, G. H., Li, G. H., Wang, Y. C., Dai, W. T.,
957   Zhang, R. J., and Zhou, Y. Q.: Mixing State of Black Carbon Aerosol in a Heavily Polluted Urban
958   Area of China: Implications for Light Absorption Enhancement, Aerosol. Sci. Technol., 48, 689-697,
959   doi: 10.1080/02786826.2014.917758, 2014.

960 Wang, Y. Q.: MeteoInfo: GIS software for meteorological data visualization and analysis,
961 Meteorological Applications, 21, 360-368, doi: 10.1002/met.1345, 2014.

962 Weingartner, E., Saathoff, H., Schnaiter, M., Streit, N., Bitnar, B., and Baltensperger, U.: Absorption
963 of light by soot particles: determination of the absorption coefficient by means of aethalometers, J.
964 Aerosol. Sci., 34, 1445-1463, doi: 10.1016/S0021-8502(03)00359-8, 2003.

965 Weyant, C. L., Shepson, P. B., Subramanian, R., Cambaliza, M. O. L., Heimburger, A., McCabe, D.,
966 Baum, E., Stirm, B. H., and Bond, T. C.: Black Carbon Emissions from Associated Natural Gas Flaring,
967 Environ. Sci. Technol., 50, 2075-2081, doi: 10.1021/acs.est.5b04712, 2016.

968 Wild, M.: Enlightening Global Dimming and Brightening, B Am Meteorol Soc, 93, 27-37, doi:
969 10.1175/bams-d-11-00074.1, 2011.

970 Wu, C., Ng, W. M., Huang, J., Wu, D., and Yu, J. Z.: Determination of Elemental and Organic Carbon
971 in PM2.5 in the Pearl River Delta Region: Inter-Instrument (Sunset vs. DRI Model 2001
972 Thermal/Optical Carbon Analyzer) and Inter-Protocol Comparisons (IMPROVE vs. ACE-Asia
973 Protocol), Aerosol. Sci. Technol., 46, 610-621, doi: 10.1080/02786826.2011.649313, 2012.

974 Wu, C., Huang, X. H. H., Ng, W. M., Griffith, S. M., and Yu, J. Z.: Inter-comparison of NIOSH and
975 IMPROVE protocols for OC and EC determination: implications for inter-protocol data conversion,
976 Atmos. Meas. Tech., 9, 4547-4560, doi: 10.5194/amt-9-4547-2016, 2016a.

977 Wu, C. and Yu, J. Z.: Determination of primary combustion source organic carbon-to-elemental carbon
978 (OC/EC) ratio using ambient OC and EC measurements: secondary OC-EC correlation minimization
979 method, Atmos. Chem. Phys., 16, 5453-5465, doi: 10.5194/acp-16-5453-2016, 2016.

980 Wu, Cheng: Aethalometer data processor, , doi:10.5281/zenodo.832404, 2017a.

981 Wu, Cheng: Minimum R Square Method (MRS), , doi:10.5281/zenodo.832396, 2017b.

982 Wu, Cheng: Histbox, , doi:10.5281/zenodo.832411, 2017c.

983 Wu, Cheng: Scatter Plot, , doi:10.5281/zenodo.832417, 2017d.

984 Wu, Cheng: Mie Scattering, , doi:10.5281/zenodo.832400, 2017e.

985 Wu, D., Mao, J. T., Deng, X. J., Tie, X. X., Zhang, Y. H., Zeng, L. M., Li, F., Tan, H. B., Bi, X. Y.,
986 Huang, X. Y., Chen, J., and Deng, T.: Black carbon aerosols and their radiative properties in the Pearl
987 River Delta region, Sci China Ser D, 52, 1152-1163, doi: 10.1007/s11430-009-0115-y, 2009.

988 Wu, D., Wu, C., Liao, B., Chen, H., Wu, M., Li, F., Tan, H., Deng, T., Li, H., Jiang, D., and Yu, J. Z.:
989 Black carbon over the South China Sea and in various continental locations in South China, Atmos.
990 Chem. Phys., 13, 12257-12270, doi: 10.5194/acp-13-12257-2013, 2013.

991 Wu, Y., Zhang, R., Tian, P., Tao, J., Hsu, S. C., Yan, P., Wang, Q., Cao, J., Zhang, X., and Xia, X.:
992 Effect of ambient humidity on the light absorption amplification of black carbon in Beijing during
993 January 2013, Atmos. Environ., 124, Part B, 217-223, doi: 10.1016/j.atmosenv.2015.04.041, 2016b.

994 Yang, M., Howell, S. G., Zhuang, J., and Huebert, B. J.: Attribution of aerosol light absorption to black
995 carbon, brown carbon, and dust in China - interpretations of atmospheric measurements during EAST-
996 AIRE, Atmos. Chem. Phys., 9, 2035-2050, 2009.

997 Yu, H., Wu, C., Wu, D., and Yu, J. Z.: Size distributions of elemental carbon and its contribution to
998 light extinction in urban and rural locations in the pearl river delta region, China, Atmos. Chem. Phys.,
999 10, 5107-5119, doi: 10.5194/acp-10-5107-2010, 2010.

1000   Yuan, J. F., Huang, X. F., Cao, L. M., Cui, J., Zhu, Q., Huang, C. N., Lan, Z. J., and He, L. Y.: Light
1001   absorption of brown carbon aerosol in the PRD region of China, Atmos. Chem. Phys., 16, 1433-1443,
1002   doi: 10.5194/acp-16-1433-2016, 2016.
1003   Zhang, G., Bi, X., Qiu, N., Han, B., Lin, Q., Peng, L., Chen, D., Wang, X., Peng, P., Sheng, G., and
1004   Zhou, Z.: The real part of the refractive indices and effective densities for chemically segregated
1005   ambient aerosols in Guangzhou measured by a single-particle aerosol mass spectrometer, Atmos.
1006   Chem. Phys., 16, 2631-2640, doi: 10.5194/acp-16-2631-2016, 2016a.
1007   Zhang, R. Y., Khalizov, A. F., Pagels, J., Zhang, D., Xue, H. X., and McMurry, P. H.: Variability in
1008   morphology, hygroscopicity, and optical properties of soot aerosols during atmospheric processing, P
1009   Natl Acad Sci USA, 105, 10291-10296, 2008.
1010   Zhang, Y., Zhang, Q., Cheng, Y., Su, H., Kecorius, S., Wang, Z., Wu, Z., Hu, M., Zhu, T.,
1011   Wiedensohler, A., and He, K.: Measuring the morphology and density of internally mixed black carbon
1012   with SP2 and VTDMA: new insight into the absorption enhancement of black carbon in the atmosphere,
1013   Atmos. Meas. Tech., 9, 1833-1843, doi: 10.5194/amt-9-1833-2016, 2016b.

1014

1015

1016   Table 1. Abbreviations.

1017

Abbreviation	Definition
$AAE_{470-660}$	Absorption Angstrom Exponent between 470 and 660 nm
BB	Biomass burning
BrC	Brown Carbon
D_{core}, D_{shell}	Particle diameter of core/shell
E_{abs550}	Light absorption enhancement factor at 550 nm
$\sigma_{abs}550$	Light absorption coefficient at 550 nm
$\sigma_{abs,t}$	Total light absorption coefficient of a coated particle
$\sigma_{abs,p}$	Primary light absorption coefficient attributed to the soot core alone of a coated particle
$\sigma_{abs,c}$	Extra light absorption coefficient due to the lensing effect of coating on the soot core
LII	Laser induced incandescence technique for soot measurement
LWC	Liquid water content
MAE_{550}	Mass absorption efficiency at 550 nm, also known as mass absorption cross-section (MAC)
$MAE_{p,550}$	Primary MAE of freshly emitted soot particles at 550 nm
MAAP	Multi Angle Absorption Photometer
MOUDI	Micro Orifice Uniform Deposit Impactor
MRS	Minimum R squared method
PAS	Photo acoustic spectrometer
PRD	Pearl River Delta region, China
SP2	Single particle soot photometer
SSA	Single scattering albedo
TD	Thermal denuder
TOA	Thermal optical analysis
TSV	Total spatial variance in backward trajectories cluster analysis

1018

1019   Table 2. Comparison of MRS application on $(OC/EC)_p$ (for SOC estimation) and MAE_p (for E_{abs} estimation).

1020

	MRS in EC tracer method for SOC estimation (Wu and Yu, 2016)	MRS in EC tracer method for E_{abs} estimation (this study)
Key parameter of fresh EC particles to be determined	$(\frac{OC}{EC})_p = \frac{POC}{EC}$	$MAE_p = \frac{O\sigma_{abs,p}}{EC}$
Input quantities for MRS from measurements	OC, EC (tracer)	$\sigma_{abs,t}$, EC (tracer)
Variable to be decoupled by the tracer	OC=POC+SOC $=(\frac{OC}{EC})_p \times EC + SOC$	$\sigma_{abs,t} = \sigma_{abs,p} + \sigma_{abs,c}$ $=(\frac{O\sigma_{abs,t}C}{EC})_p \times EC + \sigma_{abs,c}$
Ambient measurement at its closest to fresh emissions	Minimum R^2 (SOC, EC) $SOC = OC - (\frac{OC}{EC})_p \times EC$	Minimum R^2 ($\sigma_{abs,c}$, EC) $\sigma_{abs,c} = \sigma_{abs,t} - MAE_p \times EC$
Graph		

1021

1022   Table 3. Comparison of E_{abs} between various studies.

1023

Location	Type	Sampling Duration	λ (nm)	Instrument	E_{abs}	Method	Reference
Guangzhou, China	Suburban	2012.2-2013.1	550	AE+OCEC	1.50±0.48	MAE	This study
Xi'an, China	Urban	2012.12-2013.1	870	PAS	1.8	MAE	(Wang et al., 2014)
Shenzhen, China	Urban	2011.8-9	532	PAS	1.3	MAE	(Lan et al., 2013)
Jinan, China	Urban	2014.2	678	OCEC	2.07 ± 0.72	AFD	(Chen et al., 2017)
Nanjing, China	Suburban	2012.11	532	PAS	1.6	MAE	(Cui et al., 2016a)
Boulder, USA	Forest fire	2010.9	532	PAS	1.38	TD 200°C	(Lack et al., 2012a)
London, UK	Rural	2012.2	781	PAS	1.4	TD 250°C	(Liu et al., 2015)
California, USA	Rural	2010.6	532	PAS	1.06	TD 250°C	(Cappa et al., 2012)
Noto Peninsula, Japan	Rural	2013.4-5	781	PAS	1.22	TD 300°C	(Ueda et al., 2016)
Yuncheng, China	Rural	2014.6-7	678	OCEC	2.25 ± 0.55	AFD	(Cui et al., 2016b)
San Jose, Costa Rica	Rural	2006 winter	1064	SP2	1.3	Mie+SP2	(Schwarz et al., 2008)

1024   AE: Aethalometer ; OCEC: OCEC analyzer; PAS: photo acoustic spectrometer; SP2: Single particle soot photometer; TD: Thermal

1025   denuder AFD: filter filtration-dissolution

1026
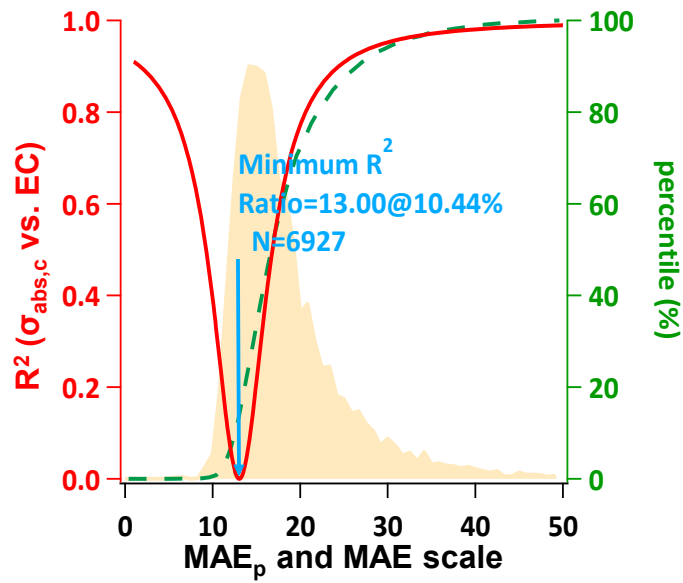
1027

Figure 1. Minimum R squared (MRS) plot for calculating MAE_p at 550 nm. The red curve is the correlation result between $\sigma_{abs,c}$ ($\sigma_{abs,t}$ – EC * MAE_p) and EC mass. The shaded area in light tan represents the frequency distribution of observed MAE. The dashed green line is the cumulative distribution of observed MAE.

1031

1032 Figure 2. Mie simulated size dependency of soot particles $AAE_{470-660}$. (a) Combination of different clear shell (y axis) and

1033 core diameters (x axis). The color coding represents the $AAE_{470-660}$ of a particle with specific core and clear shell size; (b)

1034 Cross-sections views of (a). The color coding represents different D_{core} in the range of 50 ~ 300 nm. (c)&(d) Similar to

1035 (a)&(b) but from the brown shell scenario.
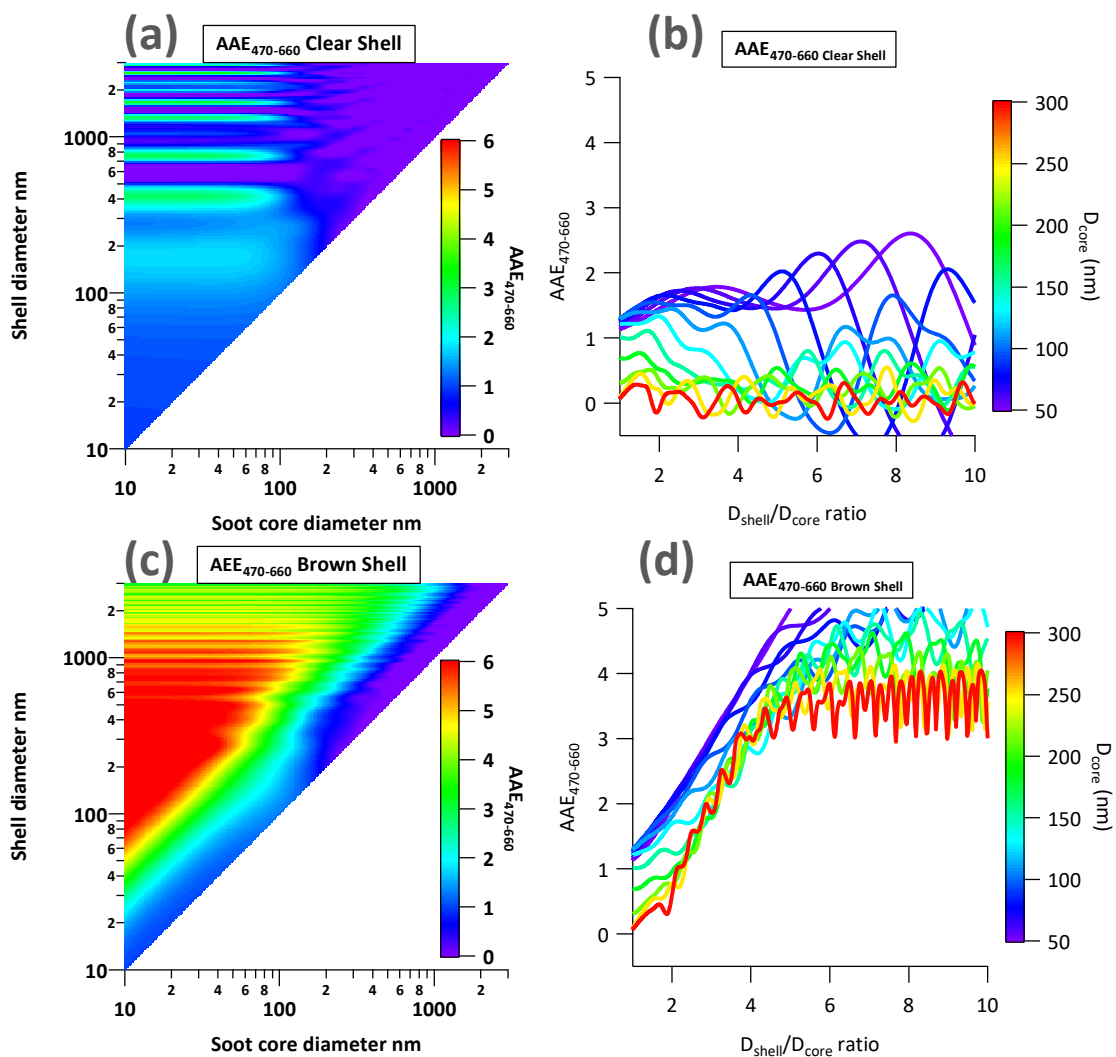
1036

1037

1038

Figure 3. Mie simulated size dependency of soot particles E_{abs} at wavelength 550 nm. (a) Combination of different clear shell (y axis) and core diameters (x axis). The color coding represents the E_{abs} of a particle with specific core and clear shell size; (b) Cross-sections views of (a). The color coding represents different D_{core} in the range of 50 – 300 nm. (c)&(d) Similar to (a)&(b) but from the brown shell scenario.
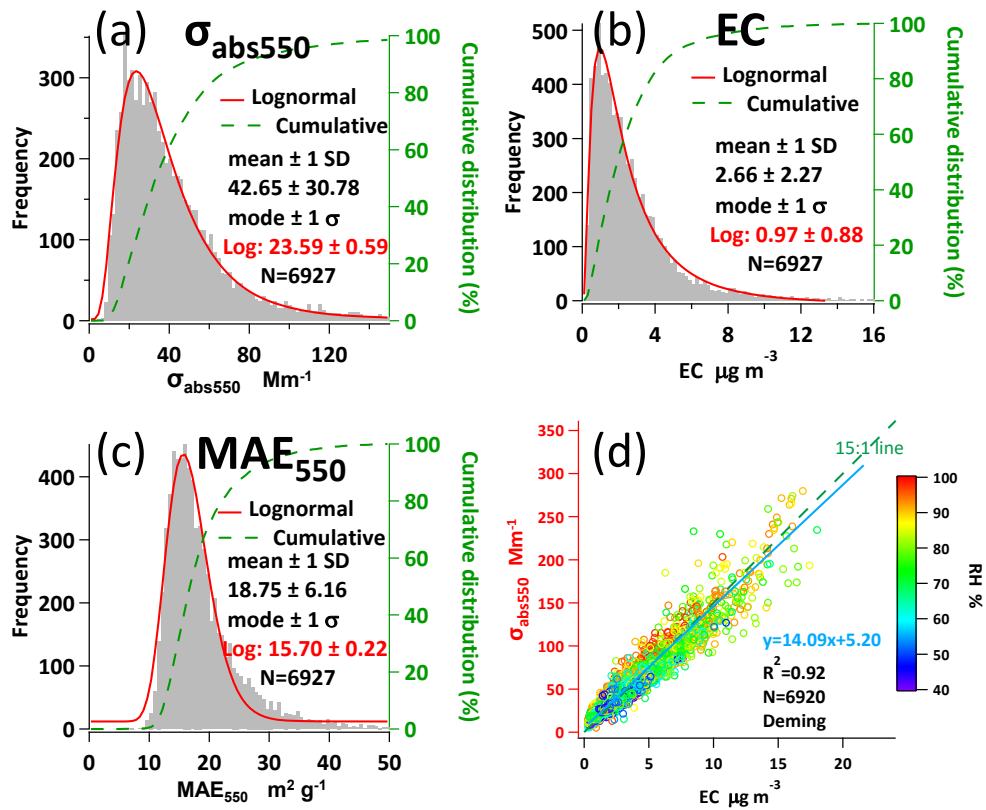
1047

Figure 4. Measured annual statistics of σ_{abs550} , EC and MAE$_{550}$. (a) Annual frequency distribution of light absorption at
550 nm. The red curve represents the fitting line for a log-normal distribution. (b) Annual frequency distribution of EC
mass concentration (c) Frequency distribution of Mass absorption efficiency (MAE) at 550 nm. (d) Scatter plot of light
absorption (550 nm) and EC mass. The slope represents MAE$_{550}$. The blue regression line is by Deming regression. The
color coding represents RH.
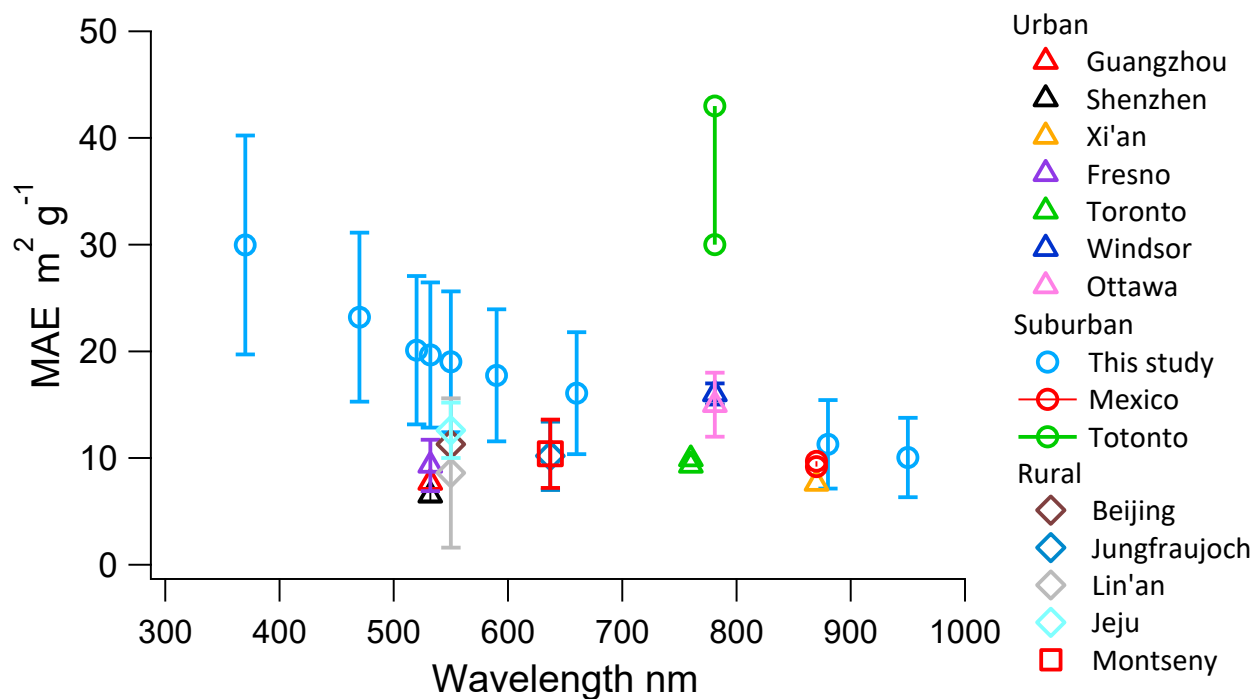
1054

Figure 5. Comparison of spectral MAE measurements from this study with previous studies. Triangle, circle and rhombus

1055 represent urban, suburban and rural respectively. Details and reference can be found in Table S1. The whiskers represent

1056 one standard deviation.

1057
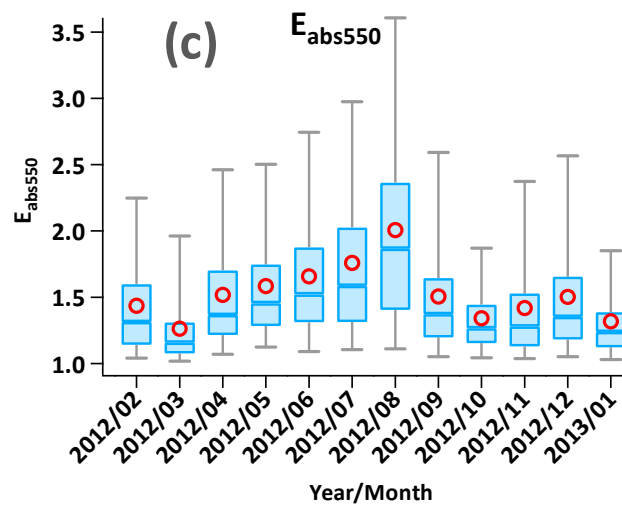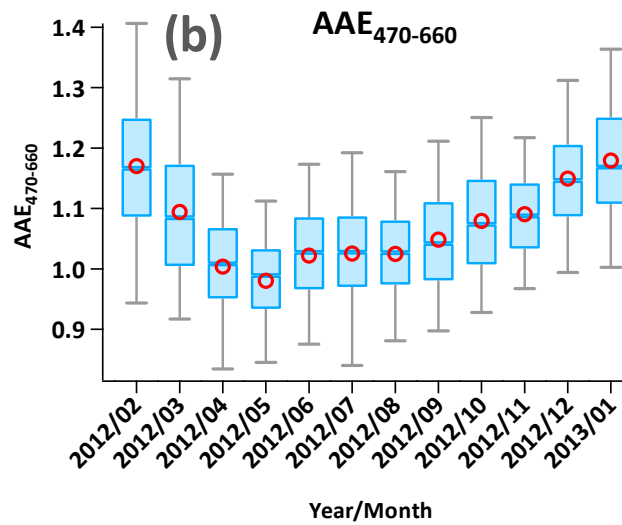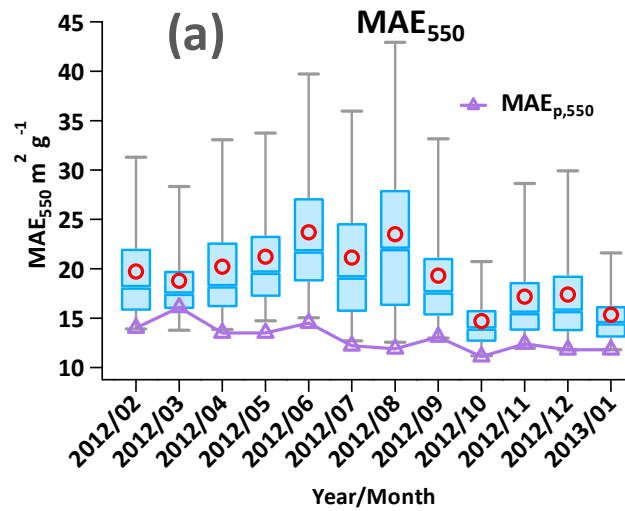
1058

Figure 6. Measured monthly variations of (a) MAE_{550}, the purple line represents $MAE_{p,550}$ estimated by MRS (b) $AAE_{470-660}$ and (c) E_{abs550}. Red circles represent the monthly average. The line inside the box indicates the monthly median. Upper and lower boundaries of the box represent the 75th and the 25th percentiles; the whiskers above and below each box represent the 95th and 5th percentiles.
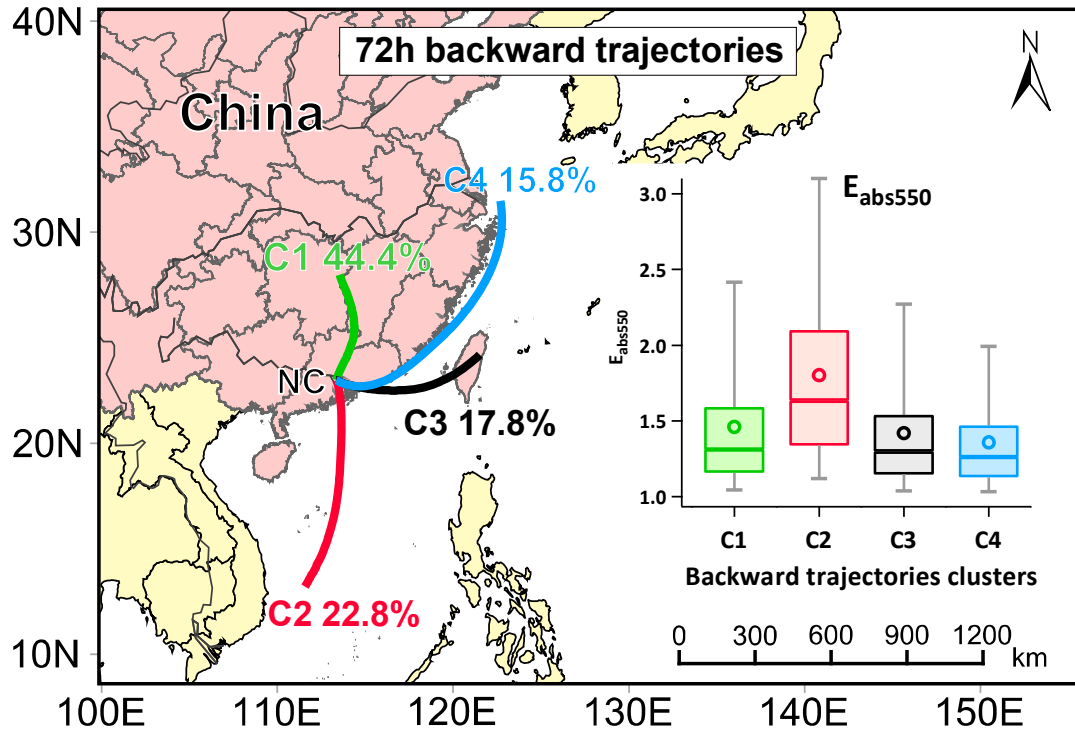
1063

Figure 7. Average backward trajectories arriving at 100 m at NC site for four clusters (2012 Feb - 2013 Jan). E_{abs550} by
different clusters are shown in the box plot.
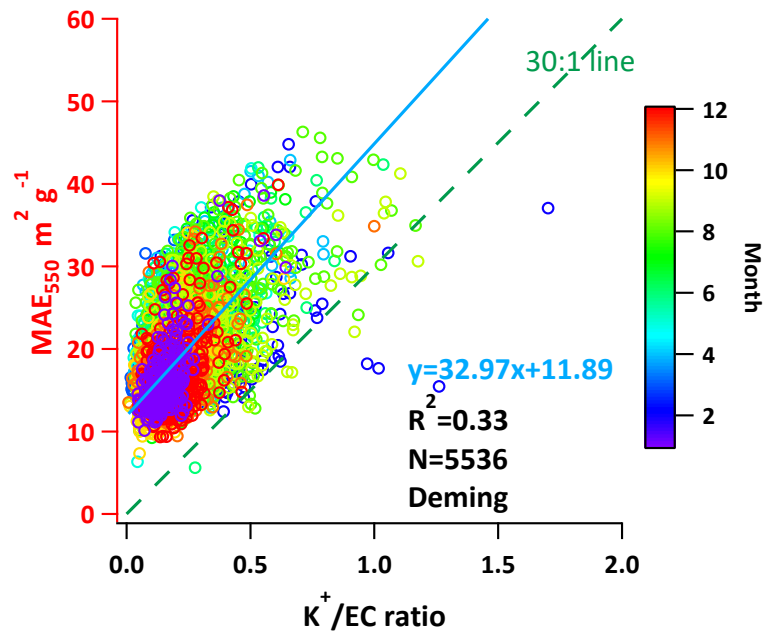
1066

1067 Figure 8. MAE_{550} dependency on biomass burning indicator K^+/EC ratio. The color coding represents months. The intercept

1068 represents MAE without biomass burning effect. The 30:1 line serves as a reference line with an integer slope that

1069 is close to the regressed slope through the origin.
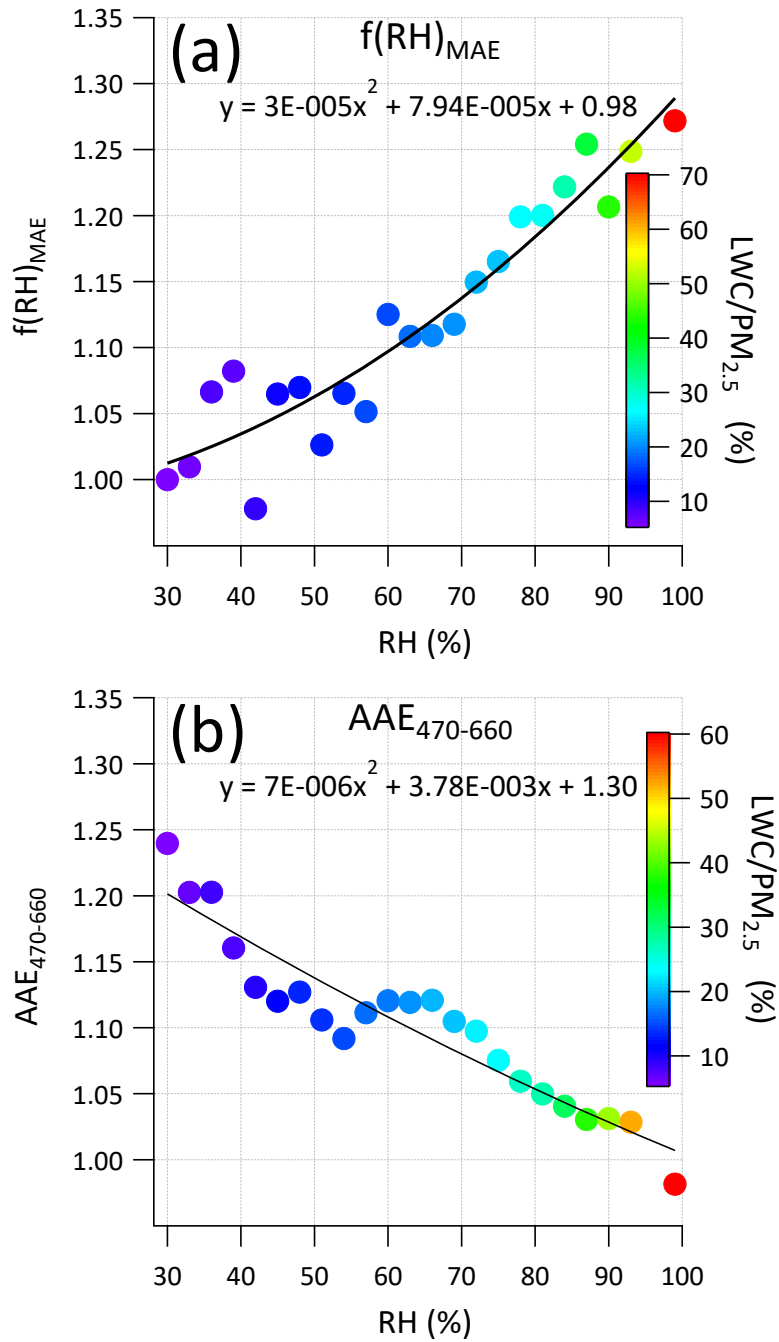
1070

Figure 9. Optical properties dependency on RH determined from one year's sampling data at NC site. (a) Hygroscopic
growth factor (f(RH)) of EC MAE_{550} (b) $AAE_{470-660}$ as a function of RH.